

Radial dependence of ionization clustering around a gold nanoparticle

Leo Thomas*, Miriam Schwarze, Hans Rabus

Physikalisch-Technische Bundesanstalt (PTB), Abbestr. 2-12, D-10587 Berlin, Germany

* E-mail: leo.thomas@ptb.de

Abstract

Objective: This work explores the enhancement of ionization clusters around a gold nanoparticle (NP), indicative of the induction of DNA lesions, a potential trigger for cell-death.

Approach: Monte Carlo track structure simulations were performed to determine (a) the fluence of incident photons and electrons in water around a gold NP under charged particle equilibrium conditions and (b) the density of ionization clusters produced on average as well as conditional on the occurrence of at least one interaction in the nanoparticle using Associated Volume Clustering. Absorbed dose was determined for comparison with a recent benchmark intercomparison. Reported quantities are normalized to primary fluence, allowing to establish a connection to macroscopic dosimetric quantities.

Main results: The modification of the electron fluence spectrum by the gold NP is minor and mainly occurs at low energies. The net fluence of electrons emitted from the NP is dominated by electrons resulting from photon interactions. Similar to dose enhancement, increased ionization clustering is limited to a distance from the NP surface of up to 200 nm. Smaller NPs cause noticeable peaks in the conditional frequency of clusters at distances around 50 nm to 100 nm from the NP surface. The number of clusters per energy imparted is increased at distances of up to 150 nm, and accordingly the enhancement in clustering notably surpasses that of dose enhancement.

Significance: This work highlights the necessity of nanodosimetric analysis and suggests increased ionization clustering near the nanoparticles due to the emission of low energy Auger electrons. Whereas the electron component of the radiation field plays an important role in determining the background contribution to ionization clustering and energy imparted, the dosimetric effects of nanoparticles are governed by the interplay of secondary electron production by photon interaction (including low energy Auger electrons) and their ability to leave the nanoparticle.

1 Introduction

In radiation therapy of tumors, well-established strategies to expand the therapeutic window are to optimize tumor conformity to the tumor volume and increase the tumor's susceptibility to irradiation. This can be done by either selectively enhancing the absorbed dose or increasing the tumor cells' sensitivity to irradiation, respectively. The introduction of gold nanoparticles (NPs) into the targeted region has been proposed as a means to achieve in both goals and has been explored in both in-vitro and in-vivo trials on mice (Hainfeld et al., 2013).

The augmentation effect is particularly manifest in X-ray-based treatment where the presence of gold NPs leads to a two-fold effect: an increase of the average dose to the tumor volume for the same fluence of incident photons and a locally increased dose in the proximity of the gold NP at distances of up to 200 nm from the nanoparticle surface (McMahon et al., 2011; Rabus et al., 2019, 2021b). While the average dose enhancement is predominantly induced by the generation of photo- and Compton electrons within the gold NP, the proximal effect is attributed to de-excitation cascades, following the emission of a photoelectron, which give rise to Auger(-Meitner) electrons with energies below 15 keV (L and M shells) (K shell vacancies are predominantly filled by fluorescence transitions creating L shell vacancies (Perkins et al., 1991).)

The spatial distribution of energy imparted in the vicinity of an interacting nanoparticle is determined by multiple factors such as nanoparticle size (Koger and Kirkby, 2016; McMahon et al., 2011; Zygmanski et al., 2013), coating (Belousov et al., 2019; Morozov et al., 2018) and the fluence of incident photons. The fluence-dependence is two-fold: the probability of a photon interaction in a gold NP is proportional to the total fluence (Zygmanski et al., 2013) and the proportionality factor depends qualitatively on the energy distribution of incident photons (Kolyvanova et al., 2021). Notably, the proximal and peripheral effect depend on these factors distinctively, cf. the ‘dichotomous nature’ of nanoparticle size described in Gadoue et al. (2018).

With respect to the proximal effect, previous studies have focused on the spatial distribution of energy imparted (or related quantities as the local dose enhancement factor) (Mesbahi, 2010; Moradi et al., 2020; Rabus et al., 2021b; Vlastou et al., 2020; Zygmanski and Sajo, 2016) or dose spikes (Lin et al., 2015; Pognant et al., 2021). However, DNA lesion clusters have been identified as a driving factor of cell-death inducing damage (Lomax et al., 2013). While DNA lesion clustering has gathered more attention in the context of high-LET radiation (cf. (Rucinski et al., 2021)), low-energy electrons such as Auger-Meitner electrons may similarly lead to a local increase in ionization clusters.

While DNA lesions can be studied at the cellular level with immunofluorescence assays (Gonon et al., 2019) and electron microscopy (Lorat et al., 2015), measuring ionization clustering, directly as a physical phenomenon, is restricted to experiments simulating nanometric volumes exploiting density scaling principles (Bantsar et al., 2017). Investigations using Monte Carlo simulations to realistically model radiation interactions around a gold NP with feasible efficiency are challenging and require the application of variance reduction techniques.

Such simulations have been performed in a multi-step paradigm, where in a first simulation the fluence at the nanoparticle is determined in water, after which radiation transport within the gold nanoparticle and the ensuing effects in the water surrounding it are simulated (in one or two steps) (Lin et al., 2014; Velten and Tome, 2023). Typically, phase-space files are employed to interface the different simulations (Klaproth et al., 2021).

While also employing a two-step approach, this work differs from previous studies in several aspects. First of all, a nanodosimetric perspective is taken by investigating the spatial distribution of ionization clusters (cf. Section 2.1), rather than energy imparted alone. Second, in the preliminary simulation step, energy distributions of photons and electrons are determined by scoring step lengths in a region of interest to obtain the spectral fluences of the two particle types without the need for manipulating phase-space files. Third, track-structure simulation is used for electron transport and the simulation setup is such that charged particle equilibrium (CPE) conditions are fulfilled. A lack of CPE could otherwise lead to significantly biased results (Rabus, 2024a; Rabus et al., 2019, 2021a). Beyond previous efforts, the photon- and electron fluences impinging on the nanoparticle are studied individually and for different nanoparticle sizes with radii ranging from 1 nm to 50 nm to better understand the physical mechanisms of the proximal and peripheral effects.

Finally, all evaluated target quantities (fluence on the nanoparticle surface, radial dependencies of frequencies of ionization clusters and energy imparted) are strictly normalized to the source fluence¹. This allows establishing a link between the local effects investigated and macroscopic average dose.

The methodology employed in this work is laid out in Section 2. After detailing the nanodosimetric perspective taken in Section 2.1, an account for the two-step simulation procedure as well as the ionization clustering procedure is given in Sections 2.2 and 2.3, respectively. Section 2.4 is dedicated to the normalization to primary fluence and establishing nomenclature not covered in Section 2.1. The results are presented in Section 3, followed by a discussion and conclusion in Section 4.

2 Methods

2.1 Nanodosimetry

Conventional dosimetry, focussing on macroscopic averages like absorbed dose (the mean imparted energy per mass (Seltzer et al., 2011)), proves reliable on larger scales. However, target sizes for the initial biophysical radiation action that leads to cell death have been identified as being of nanometric dimensions (Goodhead, 1994, 2006) and damage to cells is largely caused by local lesion clusters on DNA segments, formed over a few nanometers (Hill, 2020; Lomax et al., 2013).

¹ Note: Given the two simulation steps, confusion may arise regarding terms like ‘source’ and ‘primary’ fluence. Unless specified otherwise, these terms will refer to the fluence used in the first simulation step and symbols will carry an appropriate index, as delineated in Section 2.4.

For volumes on this scale, the stochastic nature of radiation interaction dominates and concepts like local secondary particle equilibrium or the use of an average energy per ionization to convert from ionization to energy imparted are inapplicable (Amols et al., 1990). Therefore, nanodosimetry analyzes the ionization component of charged particle track structure, the stochastic pattern of ionizing (or exciting) interactions along a particle trajectory. Classically, nanodosimetry studies the probabilities of encountering a certain number of ionizations ν , the ionization cluster size (ICS), within a specific volume at a certain position relative to a passing track (Grosswendt, 2006).

The central quantity is the probability distribution of ICS, termed ionization cluster size distribution (ICSD) and denoted as f_ν . Derived metrics such as the moments of the distribution

$$M_k(Q) \equiv \sum_{\nu \in \mathbb{N}^0} \nu^k f_\nu \quad (1)$$

and the complementary cumulative frequencies

$$F_k(Q) \equiv \sum_{\nu \geq k} f_\nu, \quad (2)$$

are extracted from this distribution. For instance, the probability that an ionization cluster of size $\nu \geq 4$ is produced conditional on the occurrence of an ionization within the sampling volume is F_4/F_1 .

Rather than adopting this traditional, probability-based perspective for a single target volume, this work adopts the conceptually different perspective of (Selva et al., 2018), focussing on total frequency N_{F_k} of clusters of size $\nu \geq k$ per primary fluence ϕ_0 in a larger, macroscopic volume (or their corresponding spatial density):

$$\frac{N_{F_k}}{\phi_0}, \quad (3)$$

with the index F_k alluding to the complementary cumulative frequency identifying the cluster.

2.2 Simulation

The simulation's aim is to obtain the spatial distribution of ionization clusters in the proximity of nanoparticles of different sizes ranging from 1 nm to 50 nm irradiated with photons of an energy spectrum corresponding to the 100-kVp X-ray spectrum used in a recent multi-center comparison of Monte Carlo simulations of dosimetric effects of a single gold NP in water (Li et al., 2020a,b)². Some details of the simulation setup used in the preliminary simulation were also chosen to allow for comparison of the results of this code to the exercise and follow-up studies (Li et al., 2020a,b; Rabus et al., 2021a,b) to be used as a reference.

A realistic track-structure simulation of a gold NP in water is not without obstacles. Two factors obstruct fast calculations. First, despite gold having a comparatively high linear attenuation coefficient, a photon traversing a gold nanoparticle is yet unlikely to interact within it (as an example, the mean number of photon interactions in a 50 nm-gold-NP (25 nm radius) irradiated with 100 kVp photons in a beam of 60 nm can be estimated to 5.4×10^{-4} per photon (Rabus et al., 2021a)).

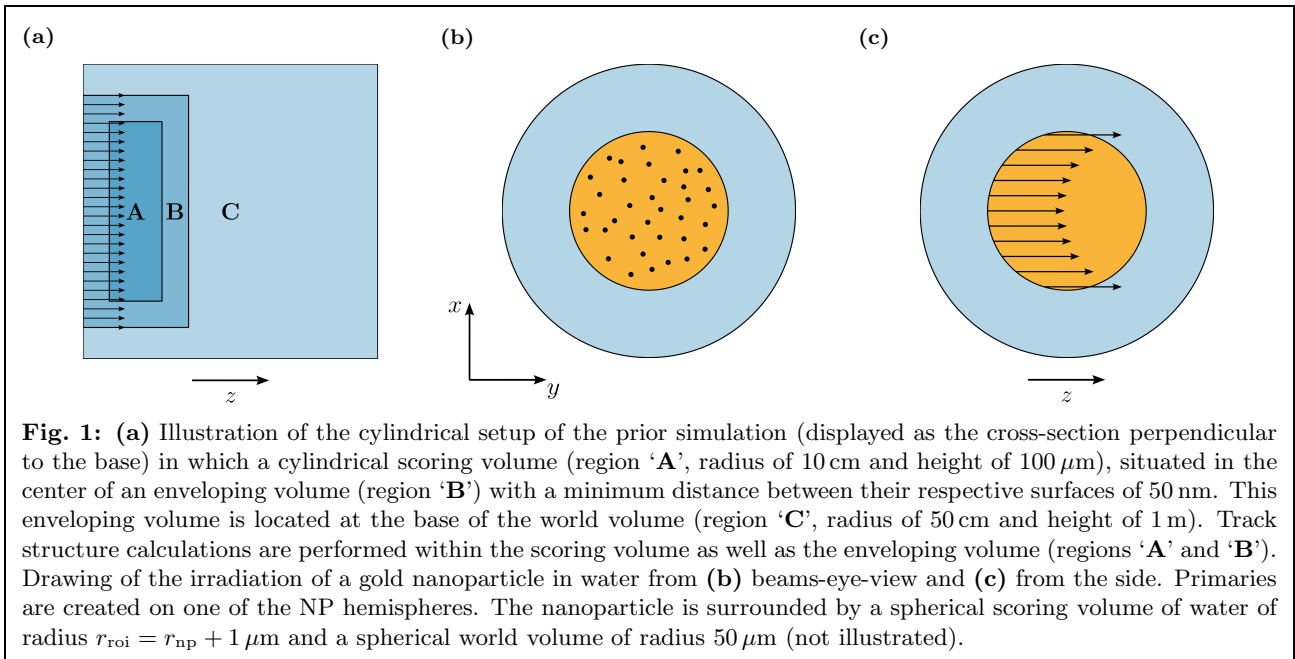
Second, produced electrons may enter or leave the region of interest (here, this is the NP and the scoring region surrounding it) and accurate simulations need to properly account for this. The explicit way to ensure this charged particle equilibrium is to increase the beam size so that the irradiated volume includes all particles that could possibly be produced and interact within the region of interest. However, this reduces the incident fluence and many produced primary particles do not contribute to tallying. In order to achieve acceptable sampling statistics for quantities differential in shells around the nanoparticle, this option is considered prohibitively inefficient.

Both of these issues can be addressed by performing the simulation in two separate steps, referred to as the prior and main simulation.

Prior simulation

In a prior simulation, the fluence of photons and secondary electrons that would be present on average at any point in a water volume (as a substitute for sub-cellular matter) where the gold NP would be located is

² It should be noted that a further (physically implausible) peak between 85.0 keV and 85.5 keV has been excluded w.r.t. the original spectrum used in Li et al. (2020b) by averaging over the two adjacent bins.



calculated. Fluence, a macroscopic quantity of course, is scored on finite areas or in finite volumes. To enhance sampling statistics, the scoring volume was chosen as a cylinder with a radius of 10 cm and a height of 100 μm , within a larger, cylindrical world volume (radius of 50 cm and height of 1 m), both aligned such that the central axis aligns with the z -axis. The wide lateral dimensions of the scoring and world volumes are to account for photons scattered back into the scoring volume by Compton or Rayleigh scattering.

For accurate results, track structure calculation was conducted both within the scoring volume, as well as within 50 μm proximity of the scoring volume to ensure equilibrium of charged particles with realistic energy spectrum throughout the entire scoring volume. A distance of 50 μm corresponds to a Continuous Slowing Down Approximation (CSDA) range of electrons in water with a kinetic energy of approximately 54.4 keV (Brice, 1984). As will become evident, roughly 97.2% of the produced secondary electrons have a kinetic energies below that. Furthermore, the CSDA range is an upper bound for the projected range, which is typically lower due to the crooked tracks of electrons.

The inner cylinder is uniformly irradiated along the longitudinal axis (see Fig. 1(a)) with photons starting at a distance of 100 μm from the center of the scoring volume (this corresponds to the interface of world volume and the volume that envelopes the scoring volume). The beam width corresponds to the lateral extension of the enveloping volume (region 'B').

Simulations were performed using the Geant4-DNA-library (Version 11.1.1) (Bernal et al., 2015; Incerti et al., 2010a,b, 2018; Sakata et al., 2019). In regions 'A' and 'B', Option 4 models were used for electron transport below 10 keV and Option 2 models above. Secondary electrons were not simulated within region 'C'. The step-lengths of the particles within the scoring volume were tallied to calculate the fluence (as described in Seltzer et al. (2011)), averaged over energy intervals of 100 eV (for photons) or in exponentially increasing intervals for electrons as motivated and outlined in Section 3.1.

Main simulation

The main simulation (or second simulation) considers a gold nanoparticle in water. In this simulation, the irradiation source is implicitly implemented by starting primary particles (photons as well as electrons, separately) on the NP surface with a distribution of kinetic energies corresponding to the photon and electron fluences obtained from the prior simulation. Following the approach of Baró et al. (1995), these energies are sampled using the Walker aliasing algorithm (Walker, 1977) for selection of the energy interval, and the kinetic energy is then uniformly sampled within this selected interval. This approach is highly efficient and allows for the generation of primary particle energies from fluence spectra provided as linear or logarithmic histograms, as done for generated photons and electrons, respectively.

The simulation setup exploits the spherical symmetry of the NP, which allows the incident particle fluence to be considered isotropic. In this implementation, all primary particles are generated on one of the NP hemispheres with equal direction of momentum (say, the z -direction) so that the projection of their point of origin along their initial direction is uniformly distributed within the plane perpendicular to that direction of momentum (the x - y -plane, see Fig. 1(c)). Radiation transport within the gold nanoparticle was simulated using the models of Sakata et al. (2019) and the electron transport in water surrounding the NP is simulated as in the prior simulation.

When performing the clustering of ionizations in a later step, only ionizations originating from the same primary (of the second simulation) are considered. This neglects the potential coincident incidence of, for instance, several electrons from the track of a higher energetic one or of a scattered photon and the related Compton electron, which are expected to be negligibly low.

In order to determine the net effect of ionization clusters and deposited energies from a gold NP (see Section 2.4), the main simulation was also performed with the gold nanoparticle absent and the corresponding volume filled with water.

Scoring

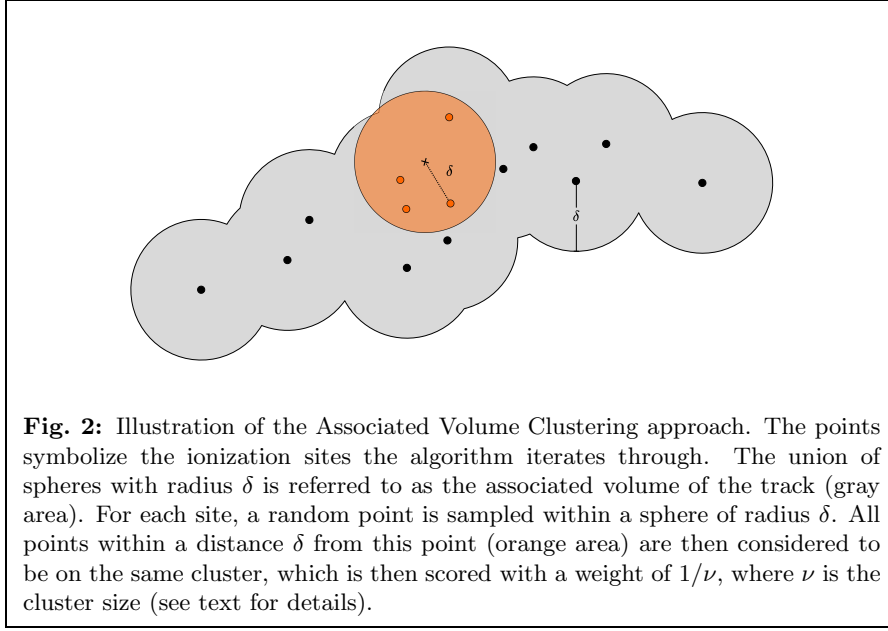
All simulation results were stored as files in the ROOT format (Brun and Rademakers, 1997) containing the energy transfer points (namely the event identifier, particle type, process type, energy deposit and coordinates) as well as step length data to score fluence (containing the event identifier, particle type, step length and kinetic energy) in a separate branch of the file. The step length data was used to score fluence in the prior simulation, whereas the fluence in the main simulation was determined by scoring only those particles traversing the NP surface and determining the fluence as the number of such particles per cross-sectional area of the nanoparticle. The ensuing data analysis (clustering, scoring of imparted energy etc.) was performed in a pipeline of dedicated C++ codes. While such data analysis is often executed at simulation time (i.e. from within the Geant4 user code), this approach offers the possibility of modifying the data analysis, if so desired, without having to re-run the simulation. Naturally, this flexibility comes at the expense of storing the raw data of ionizations and step lengths.

2.3 Clustering

In this work, ionization clusters are scored in spherical targets of 1.5 nm radius, which are equal in volume to the often used cylinders with a height of 3.4 nm and radius of 1.15 nm representing a DNA segment of ten base pairs (Grosswendt, 2006). The sampling volumes are not uniformly distributed in the entire region of interest (ROI) as, for instance, in Alexander et al. (2015) and Ramos-Méndez et al. (2018) as this is inefficient, especially for loosely ionizing particles such as photons. Instead, they are sampled within a volume enveloping the track, the track's associated volume (AV) (Kase et al., 1985, Chapter 2, by A. M. Kellerer). The associated volume of a track (gray area in Fig. 2) is the union of all spheres of radius δ centered at the loci of all n_t energy transfer points with ionizations. The AV of the track, V_t , and the AVs of the individual ionizations, V_i , can be segmented in disjoint sub-volumes, $V_{t,\nu}$ and $V_{i,\nu}$, respectively, representing the intersections of ν different spheres such that

$$V_t = \sum_{\nu} V_{t,\nu}, \quad V_i = \sum_{\nu} V_{i,\nu} \quad \text{and} \quad V_{t,\nu} = \frac{1}{\nu} \sum_{i=1}^{n_t} V_{i,\nu}. \quad (4)$$

The normalization to ν in the last identity in Eq. 4 accounts for the fact that each such intersection is counted ν times in the sum. Averaged over tracks, the $V_{t,\nu}$ are proportional to the probability of formation of an ionization cluster of size ν . The AV clustering algorithm cycles through the ionization sites of a track. For each site, a point is sampled within a sphere of radius δ . A scoring volume of the same size (orange area in Fig. 2) is placed at this point and all ionization sites within this volume are counted to establish the ionization cluster size ν , which is then counted with a weight of $1/\nu$ to account for the (potential) ν -fold counting.



2.4 Notation and Normalization

Notation

Important quantities are the fluences of the appearing radiation fields, such as the (integral) primary fluence ϕ_0 , defined as the number of particles dN_0 incident on a sphere of cross-sectional area dA (Seltzer et al., 2011)

$$\phi_0 = \frac{dN_0}{dA} \quad (5)$$

or its corresponding distribution with respect to energy $d\phi_0/dE$ (referred to as spectral fluence).

The two-step simulation approach readily allows individuating the different components of the radiation field to clustering as well as energy imparted, namely the four contributions of a primary photon causing either a photon or an electron to enter the NP (simulation I) and upon interaction a photon or an electron to leave the NP (simulation II):

$$\gamma \xrightarrow{\text{I}} \{\gamma, e^-\} \xrightarrow{\text{II}} \{\gamma, e^-\}$$

Correspondingly, the fluences are denoted as

$$\phi_0^{(\gamma)} \xrightarrow{\text{I}} \phi_1^s \xrightarrow{\text{II}} \phi_2^{s \rightarrow s'}$$

with $s, s' \in \{\gamma, e^-\}$. Namely, ϕ_1^s denotes the fluence of particles of type s (entering the nanoparticle) and $\phi_2^{s \rightarrow s'}$ denotes the fluence of particles of type s' (leaving the nanoparticle), produced by a particle of type s (entering the nanoparticle).

In order to link local effects around the nanoparticle to macroscopic quantities, such contributions need to be normalized meaningfully, for instance, to the primary fluence ϕ_0 . For the spectral fluence penetrating the nanoparticle $d\phi_1^s/dE$, this is straight-forwardly

$$\frac{1}{\phi_0} \frac{d\phi_1^s}{dE}$$

For the second simulation, this is non-trivial as different numbers of histories are simulated for photons and electrons, which do not correspond to the primary fluence. Here, the notation will distinguish between the “actual” fluences ϕ_i , which correspond to the primary radiation field in the first simulation and the fluences used in the second simulation, marked with a tilde $\tilde{\phi}_i$ (in the case of primary fluence, these two quantities simply

coincide, i.e. $\phi_0 = \tilde{\phi}_0$). The fluence $\phi_2^{s \rightarrow s'}$ depends on the fluence ϕ_1^s via $p^{s \rightarrow s'}(E'|E)$, the expectation of the number of particles of type s' and energy E' that are produced when a particle of type s with energy E enters the nanoparticle, so that:

$$\begin{aligned} \frac{1}{\phi_0} \frac{d\phi_2^{s \rightarrow s'}}{dE'} &= \frac{1}{\phi_0} \int dE p^{s \rightarrow s'}(E'|E) \frac{d\phi_1^s}{dE} \\ &= \frac{1}{\phi_0} \frac{\phi_1^s}{\tilde{\phi}_1^s} \int dE p^{s \rightarrow s'}(E'|E) \frac{d\tilde{\phi}_1^s}{dE} \\ &= \frac{1}{\phi_0} \frac{\phi_1^s}{\tilde{\phi}_1^s} \frac{d\tilde{\phi}_2^{s \rightarrow s'}}{dE'} \end{aligned} \quad (6)$$

The same rationale can be applied for a generic quantity of interest Q (here as a linear density, as a distribution of x , for example the radial distance r from the nanoparticle center), resulting in the same normalization factor, so that:

$$\frac{1}{\phi_0} \frac{dQ}{dx} = \frac{1}{\phi_0} \frac{\phi_1^s}{\tilde{\phi}_1^s} \frac{d\tilde{Q}}{dx} \quad (7)$$

To account for the expected background contribution to a quantity of interest, the net contribution from the gold nanoparticles must be calculated, namely the surplus effect that the presence of the nanoparticle adds compared to when it is absent. For this purpose the main simulation was performed with a spherical water volume, as a stand-in for the nanoparticle, as described in Section 2.2. The difference between the gold NP contribution $Q_g^{s \rightarrow s'}(r_{\text{np}})$ and the corresponding, spherical water volume $Q_w^{s \rightarrow s'}(r_{\text{np}})$ with $s, s' \in \{\gamma, e^-\}$ for a contribution is called the net contribution

$$\frac{dQ_{\text{net}}^{s \rightarrow s'}}{dx}(r_{\text{np}}) \equiv \frac{dQ_g^{s \rightarrow s'}}{dx}(r_{\text{np}}) - \frac{dQ_w^{s \rightarrow s'}}{dx}(r_{\text{np}}), \quad (8)$$

to which the background contribution from the prior simulation is then added:

$$\frac{1}{\phi_0} \frac{dQ}{dx}(r_{\text{np}}) = \sum_{s, s' \in \{\gamma, e^-\}} \frac{1}{\phi_0} \frac{dQ_{\text{net}}^{s \rightarrow s'}}{dx}(r_{\text{np}}) + \frac{1}{\phi_0} \frac{dQ^{\text{b}}}{dx} \quad (9)$$

where r is the gold NP radius and dQ^{b} is the background contribution within the interval $[x, x + dx]$. In case that $x = r$, the radial distance from the nanoparticle center, $dQ^{\text{b}}(r) = Q^{\text{b}}/V_{\text{b}} \cdot dV(r)$ (with V_{b} the scoring volume of the prior simulation) is the contribution from the background simulation, in a volume of the spherical shell comprised within the interval $[r, r + dr]$.

Conditional normalization

The quantities determined by the identity on the right-hand side of Eq. 9 are averaged over all primary particles of the respective second simulation. For the case of incident photons, the probability of an interaction in the gold NP is relatively low. Therefore, it is interesting to look at the distribution of ionization clusters around a gold NP in which an ionizing interaction of a photon occurs. In most cases, the incident photon does not interact in the gold NP, no electrons are emitted from the gold NP and the expected cluster density around the gold NP is equal to the background contribution. If the photon interacts, the cluster density is enhanced with respect to the average cluster density obtained from the simulation. The enhancement is by a factor of $1/\bar{n}_0^\gamma(r_{\text{np}})$, where $\bar{n}_0^\gamma(r_{\text{np}}) \equiv \bar{n}^\gamma(r_{\text{np}}, \phi_0)$ is the expected number of photon interactions taking place in the gold NP with radius r_{np} for a primary photon fluence ϕ_0 .

The probability of an incident photon undergoing an ionizing interaction in the gold NP is approximately (in lowest order approximation) given by

$$\langle p_i^\gamma \rangle_{\phi_1^\gamma} = \bar{\ell} \langle \mu_{i, \text{g}} \rangle_{\phi_1^\gamma} = \frac{\bar{\ell}}{\phi_1^\gamma} \int dE \frac{d\phi_1^\gamma}{dE} \mu_{i, \text{g}}(E) \quad (10)$$

Here, $\bar{\ell} = 4r_{\text{np}}/3$ is the mean chord length (or path length) of a photon traversing the (spherical) nanoparticle, $\mu_{i,g}$ denotes the linear attenuation coefficient of gold for ionizing interactions, and $d\phi_1^\gamma/dE$ is the energy spectrum of the photons impinging on the gold NP. The photon interaction probabilities used in this work are obtained using this method. The values used of the linear attenuation coefficients are from the generalized spline-interpolation of the data from Berger et al. (2010), presented in Rabus et al. (2019). The probability of a photon interaction can also be estimated from the fluence spectra obtained in the second simulation as follows:

$$\langle p_i^\gamma \rangle_{\phi_1^\gamma} = 1 - \frac{\phi_2^{\gamma \rightarrow \gamma}(E_{\text{min}})}{\phi_1^\gamma(E_{\text{min}})} \quad \text{with} \quad \phi_i(E_{\text{min}}) \equiv \int_{E_{\text{min}}}^{\infty} dE \frac{d\phi_i}{dE} \quad (11)$$

Here E_{min} was chosen as 15 keV, which is an effective lower bound of the relevant section of the photon spectrum and excludes low-energy fluorescence photons produced within the gold NP. The two approaches to determine interaction probability (Eq. 10 and Eq. 11) yield slightly different results, which reflect the uncertainty of the cross-sections Andreo et al. (2012). A comparison of the probabilities obtained from both methods for the nanoparticle radii used in this work can be found in Supplementary Table S1.

The expected number of ionizing interactions in gold per primary fluence ϕ_0 is then given by

$$\frac{\bar{n}_0^\gamma(r_{\text{np}})}{\phi_0} = r_{\text{np}}^2 \pi \frac{\phi_1^\gamma}{\phi_0} \langle p_i^\gamma \rangle_{\phi_1^\gamma} = \frac{4\pi}{3} r_{\text{np}}^3 \frac{\phi_1^\gamma}{\phi_0} \langle \mu_{i,g} \rangle_{\phi_1^\gamma} \propto r_{\text{np}}^3 \quad (12)$$

and is proportional to the volume of the gold NP. When a quantity of interest as determined by Eq. 7 is normalized to the ratio given in Eq. 12, the result is the expected value of this quantity of interest conditional on the occurrence of a single ionizing interaction of a photon occurring in the gold NP and does not depend on the primary fluence. If the gold NP undergoes k ionizations by photons, the expected values of the conditional quantity are k times higher, again independent of primary fluence.

However, the expected number of ionizing photon interactions in a gold NP depends on the primary fluence. Therefore, the values of a quantity of interest conditional on at least one ionizing interaction occurring in the gold NP depends on the primary fluence, with different primary fluences corresponding to different ratios of the contribution of the gold NP undergoing an interaction to the background contribution. A natural choice seems to be values of primary fluence ϕ_0^D that correspond to given values of absorbed dose D , given by

$$\phi_0^D \equiv D \frac{\phi_0}{D_0} \quad (13)$$

with D_0 being the dose corresponding the the primary fluence ϕ_0 . The expected number of interactions per fluence in Eq. 12 is independent of fluence, so that

$$\frac{\bar{n}_0^\gamma}{\phi_0} = \frac{\bar{n}_D^\gamma}{\phi_0^D} \implies \bar{n}_D^\gamma \equiv \bar{n}^\gamma(D) = \phi_0^D \frac{\bar{n}_0^\gamma}{\phi_0}. \quad (14)$$

In Eq. 14 and in the following, the argument r_{np} is dropped to abridge notation.

Even though, the probability of a single photon undergoing an ionization event within a gold nanoparticle is relatively low, the number of such events occurring in a single nanoparticle aggregates for fluences corresponding to higher doses. Since interactions of different photons can be considered statistically independent, the probability of the number of interactions occurring for an expected number of interactions \bar{n}_D^γ is Poisson-distributed and the probability of k events occurring is thus given by

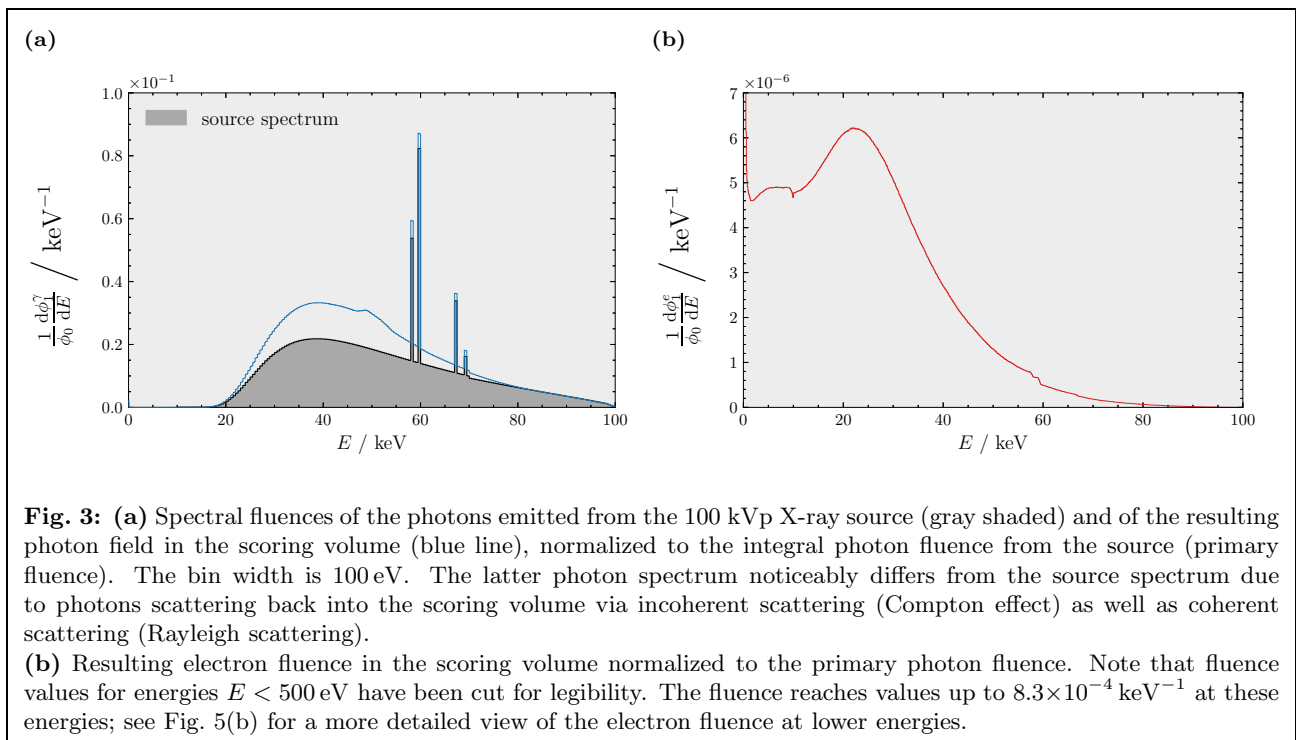
$$P(k|n_D^\gamma) = \frac{(\bar{n}_D^\gamma)^k}{k!} e^{-\bar{n}_D^\gamma}$$

and the probability of one or more ionizing events sums up to

$$P(k \geq 1|n_D^\gamma) = e^{-\bar{n}_D^\gamma} \sum_{k \in \mathbb{N}} \frac{(\bar{n}_D^\gamma)^k}{k!} = 1 - e^{-\bar{n}_D^\gamma}. \quad (15)$$

A quantity of interest Q conditional on one or more interactions occurring in a gold NP is, therefore, given by Eq. 16. The factor in front of the curly brackets is the expectation of the number of interactions conditional on the occurrence of at least one.

$$\frac{dQ_C^\gamma(D)}{dx} = \frac{\bar{n}_D^\gamma}{1 - e^{-\bar{n}_D^\gamma}} \left\{ \frac{1}{\bar{n}_0^\gamma} \frac{dQ_{\text{net}}^{\gamma \rightarrow \gamma}}{dx} + \frac{1}{\bar{n}_0^\gamma} \frac{dQ_{\text{net}}^{\gamma \rightarrow e}}{dx} \right\} + \frac{\phi_0^D}{\phi_0} \frac{dQ^b}{dx}, \quad (16)$$



Relevant quantities

Quantities of interest are the number of clusters of size $\nu \geq k$, N_{F_k} , as a function of radial distance r and the number of such clusters per mass, a quantity corresponding to the cluster dose g^{F_k} , introduced in Faddegon et al. (2023), as well as the energy ε imparted by ionizations and the corresponding dose contribution D from ionizations. A summary of the relevant quantities can be found in Supplementary Table S2.

3 Results

3.1 Fluence spectra

The fluence data obtained from the prior simulation is depicted in Fig. 3. The photon fluence in the region of interest is overall higher than that of the primary spectrum ($\phi_1^\gamma \approx 1.38 \phi_0$). This is a consequence of Compton as well as Rayleigh scattering of photons in the large simulation volume back into the region of interest (ROI). The secondary-electron fluence is significantly lower than the photon fluence ($\phi_2^e \approx 3.18 \times 10^{-4} \phi_1^\gamma$) and characterized by a continuum of photo-electrons as well as lower energetic Compton electrons at energies $\lesssim 10$ keV.

By virtue of the two-step procedure in simulation, the single contributions to the fluence leaving the nanoparticle are readily available and allow gaining a clearer perspective on the different physical processes governing the formation of ionization clusters in the nanoparticle's periphery. Most relevant to the formation of clusters are the fluences of emitted electrons produced by incident photons or electrons. Fig. 4 and Fig. 5(b) report the energy distribution of electrons on the surface of nanoparticles with different radii, distinguishing between those of electrons produced by photons $\phi_2^{\gamma \rightarrow e}$ and by electrons $\phi_2^{e \rightarrow e}$ entering the nanoparticle. The binning is logarithmic with a minimum energy of $E_{\min} = 10$ eV, and 100 bins per decade, so that the positions of the lower bin edges are given by

$$\left\{ E_{\min} \cdot 10^{k/100} \mid k \in \mathbb{N}^0 \right\}.$$

The data are plotted in ‘microdosimetry style’, whereby the linear vertical axis shows the fluence multiplied with the $\ln(10)E$. While technically the quantity shown on the y -axis is proportional to the energy fluence, this way of presentation assures that the area under the curve in any energy interval is representative of the contribution of electrons in this interval to the total number of emitted electrons.

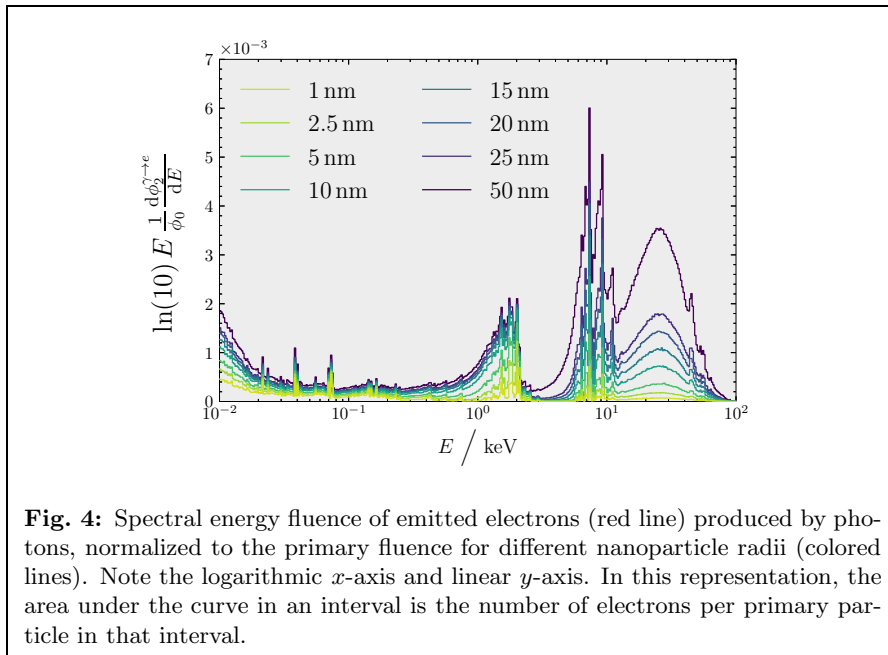


Fig. 4: Spectral energy fluence of emitted electrons (red line) produced by photons, normalized to the primary fluence for different nanoparticle radii (colored lines). Note the logarithmic x -axis and linear y -axis. In this representation, the area under the curve in an interval is the number of electrons per primary particle in that interval.

The photon-induced electron spectrum in Fig. 4 exhibits an overall dependence on nanoparticle radius r_{np} . In fact, the number of electrons leaving the nanoparticle $N_2^{\gamma \rightarrow e}$ is proportional to the mean number of photon-interactions $\bar{n}_0^\gamma(r_{\text{np}})$ within the nanoparticle, introduced in Eq. 12, so that

$$\phi_2^{\gamma \rightarrow e} = \frac{N_2^{\gamma \rightarrow e}}{A_{\text{np}}} \propto r_{\text{np}}.$$

Qualitatively, the spectra in Fig. 4 contain a continuum of photo-electrons, mainly at energies $E \gtrsim 10$ keV, and a number of partially overlapping peaks that correspond to Auger transitions. For the binning used, it may not be possible to identify all peaks individually at larger energies as two separate peaks might coalesce. Additionally, the Auger electrons are subject to some straggling on their way to the nanoparticle surface, which smears the peaks to some extent.

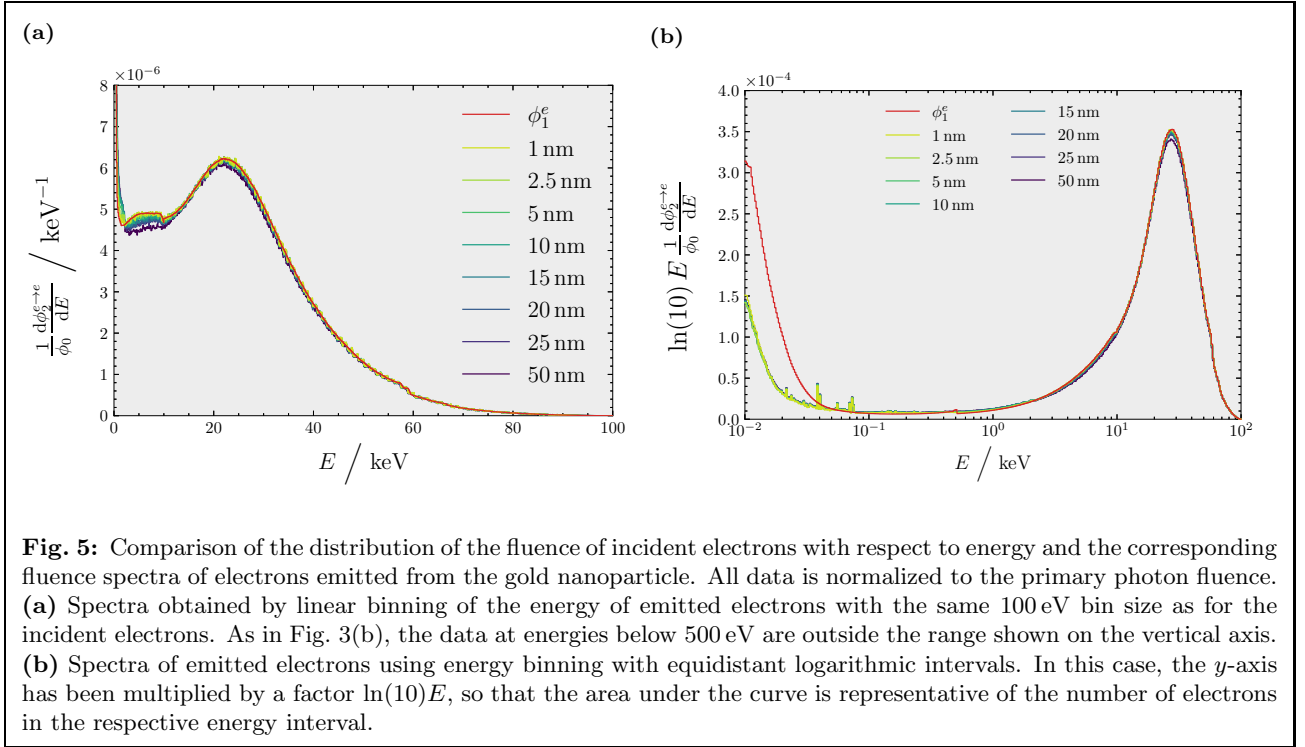
The prominent peaks at energies between 7.3-7.4 keV, 9.2-9.3 keV as well as between 11.1-11.2 keV are caused by electrons from L shell Auger transitions³. Further peaks at energies from 1.5 keV up to 2.1 keV originate from M shell Auger electrons and the peaks at lower energies can likely be associated with N or O shell transitions or Coster-Kronig transitions.

Qualitatively, the electron-induced electron fluence spectra $\phi_2^{e \rightarrow e}$ shown in Fig. 5(a) appear almost the same as the spectrum of electrons entering the nanoparticle ϕ_1^e . A minor decrease of the spectral fluence can be seen at energies above 2 keV, which is most pronounced in the energy range from 2 keV to 10 keV and can be attributed to impact ionization within the NP (for larger radii). However, the integral fluences are almost independent of radius.

Since the probability of incident electrons undergoing inelastic interactions in the gold NP decreases with decreasing gold NP size, it is expected that the energy spectra leaving the gold NP asymptotically approach the incident electron spectrum with decreasing radii. While such behavior can be observed at higher energies in both Fig. 5(a) and Fig. 5(b), the fluence spectra of emitted electrons visibly deviate from the spectral fluence of incident electrons at energies below 100 eV.

This behavior is attributed to the high probability of low energy electrons to undergo an inelastic interaction in gold (see Supplementary Fig. S1). While impact ionization by higher energy electrons predominantly leads to a production of electrons at low energies, the high probability of inelastic interactions at low energies effectively leads to an absorption of these electrons (or, more precisely, deceleration to energies below the ionization threshold of water).

³ The gold models of Geant4 (Sakata et al., 2019) used here use transition energies from the EADL database (Perkins et al., 1991).



In comparison, the $(\gamma \rightarrow e)$ -component dominates the electron fluence on the gold NP surface especially for growing nanoparticle sizes; the value of $\phi_2^{\gamma \rightarrow e} / \phi_2^{e \rightarrow e}$ grows from 1.43 ($r_{\text{np}} = 1$ nm) to 16.94 ($r_{\text{np}} = 50$ nm). For integral fluences at energies corresponding to M shell Auger electrons ($500 \text{ eV} \leq E < 5.5 \text{ keV}$), this fraction ranges from 2.90 ($r_{\text{np}} = 1$ nm) to 34.98 ($r_{\text{np}} = 50$ nm). See Supplementary Table S3 for a more detailed overview.

3.2 Ionization clustering

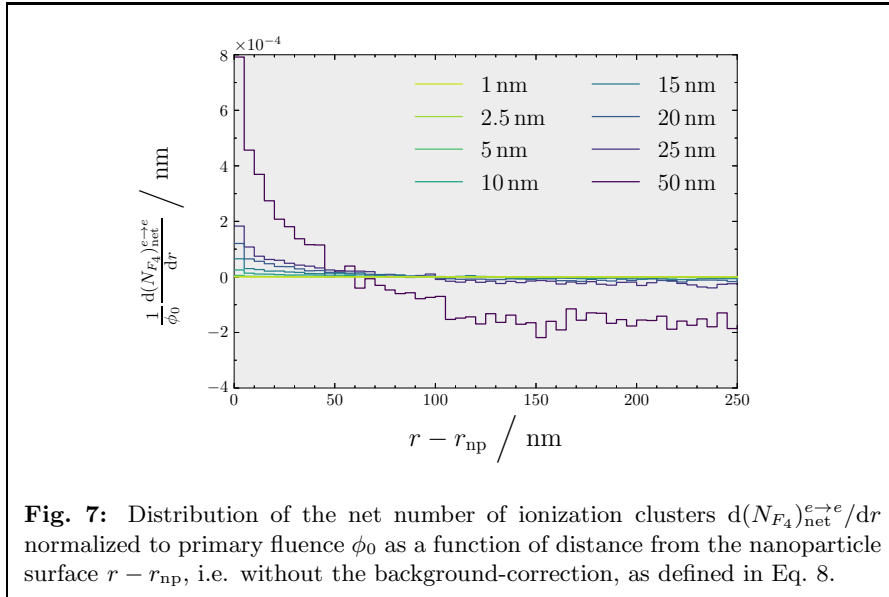
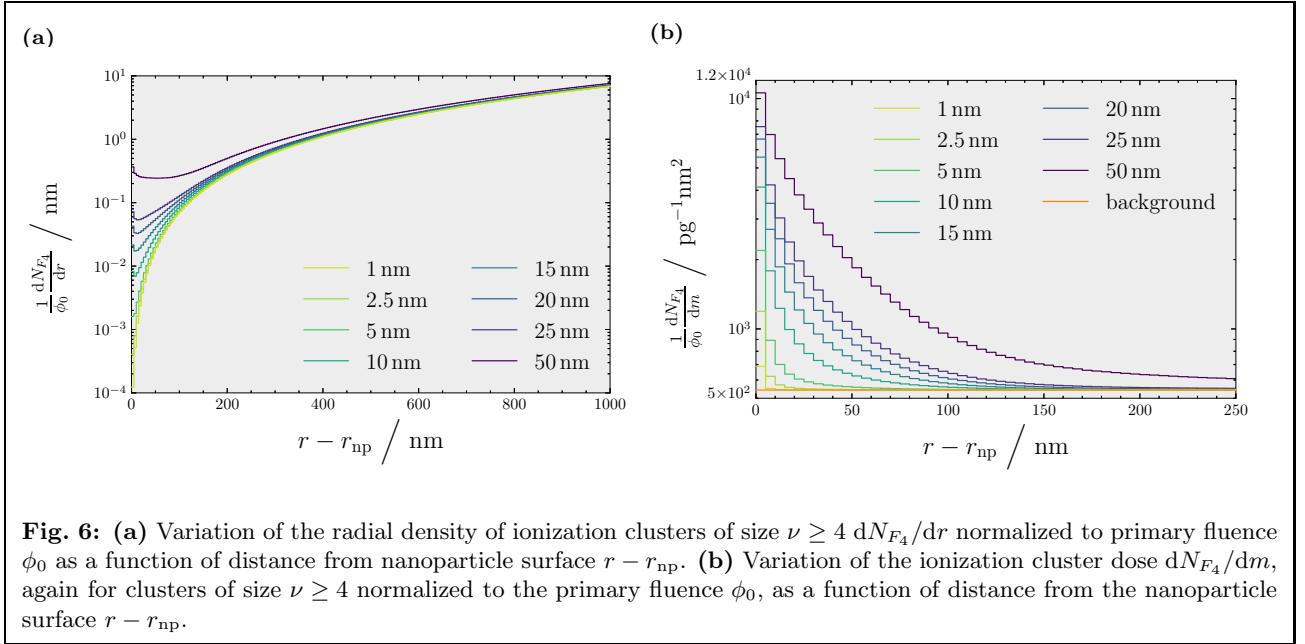
Fig. 6(a) illustrates the frequency distribution of ionization clusters of size $\nu \geq 4$ within shells surrounding the nanoparticles dN_{F_4}/dr normalized to the primary fluence ϕ_0 . The count of clusters has been corrected for contributions that occur when the gold NP is replaced by water, as outlined in Eq. 9. In alignment with the r_{np}^3 -dependence discussed in Section 3.1, the nanoparticle radius r_{np} impacts the total number of clusters created. The background contribution $dN_{F_4}^b/dr$ is proportional to the volume comprised between $[r, r + dr]$, which approximately grows with r^2 .

Fig. 7 shows the net effect of the gold nanoparticle of clusters stemming from electron impact ionizations, created by electrons entering the gold nanoparticle, $d(N_{F_4})_{\text{net}}^{e \rightarrow e}/dr$ normalized to primary fluence ϕ_0 . While the attenuation coefficients for photons differ by two or three orders of magnitude between water and gold at the photon energies of the 100 kVp spectrum used here, the stopping powers of electrons at the relevant energies are of the same order of magnitude⁴. Therefore, the gold and water-only contributions of ionization clusters almost cancel each other out. In fact, beyond distances of 60 nm - 100 nm, the water-only contribution exceeds the gold contribution, which is known for energy imparted as the sink effect (Brivio et al., 2017).

Since the absolute number of clusters from the background grows with shell volume, Fig. 6(b) displays cluster frequency per mass dm , of the corresponding shell. In this normalization, the background contribution to the resulting quantity is constant in r and the resulting quantity corresponds to the cluster dose g^{F_4} introduced by (Faddegon et al., 2023), conceptually.

The radial cluster density of photons conditional on the occurrence of at least one ionization as described by Eq. 16 is depicted in Figs. 8(a) - 8(d) for different radii ($r_{\text{np}} = 1$ nm, 5 nm, 25 nm and 50 nm) as well as three doses corresponding to different use cases: 10 mGy as a typical order of magnitude of the dose received in a CT scan, 2 Gy as a typical fraction in conventional radiation therapy as well as 50 Gy, corresponding to a

⁴ The fluence-averaged stopping-power ratio is estimated to be $\langle S_w \rangle_{\phi_1^e} / \langle S_g \rangle_{\phi_1^e} \approx 2.48$ (Brice, 1984)

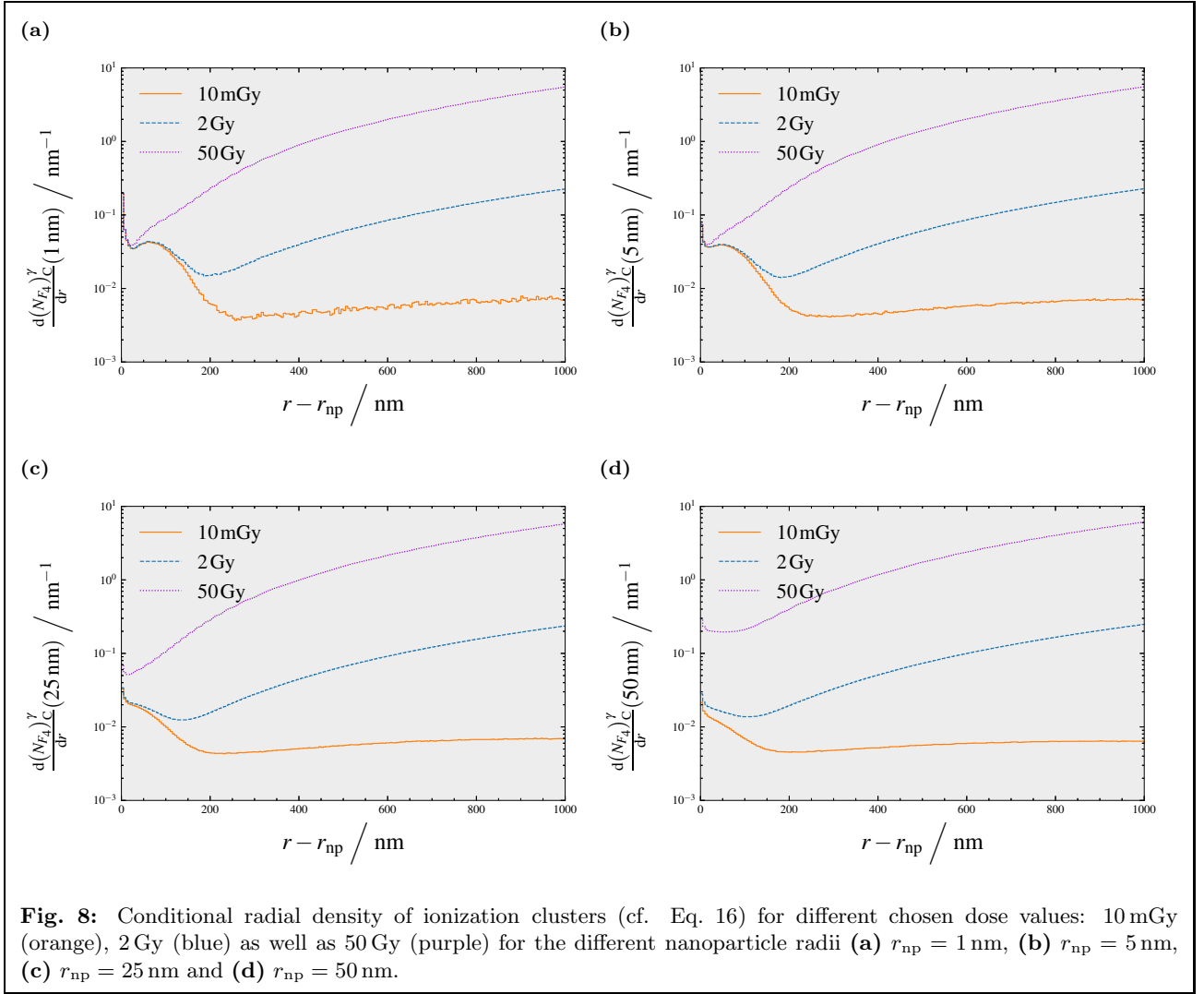


possible single dose fraction in FLASH-RT that utilizes brief (< 200 ms) irradiations with dose rates ≥ 40 Gy/s (Vozenin et al., 2019).

It becomes apparent, that the absorbed dose influences the formation of clusters in a non-linear fashion, which is a consequence of the likelihood of multiple interactions occurring, which increases with the absorbed dose, outlined in Section 2.4. This effect is especially evident for smaller gold NPs, where a shoulder pattern emerges for distances of roughly up to 200 nm from the nanoparticle surface. Judging from this distance, these clusters are caused by low energy electrons, namely the M shell Auger electrons visible in the photon-generated electron spectrum in Fig. 4.

3.3 Imparted energy and dose

The imparted energy per radial shell, illustrated in Fig. 9(a), as well as the absorbed dose (Fig. 9(b)) per primary fluence ϕ_0 as a function of radial distance from the nanoparticle surface qualitatively correspond to the ionization cluster density and cluster dose (Figs. 6(a) and (b), respectively) and display the same r_{np}^3 -dependence



discussed earlier.

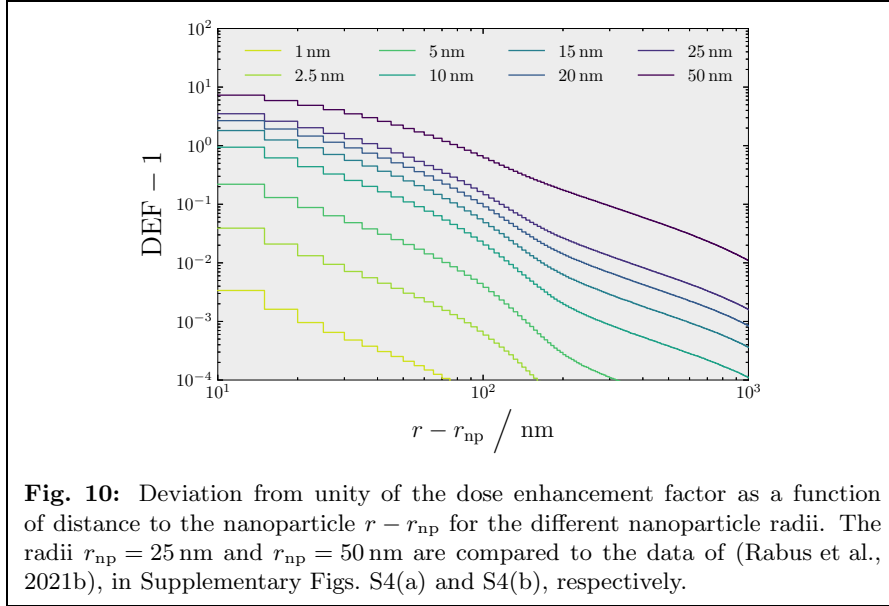
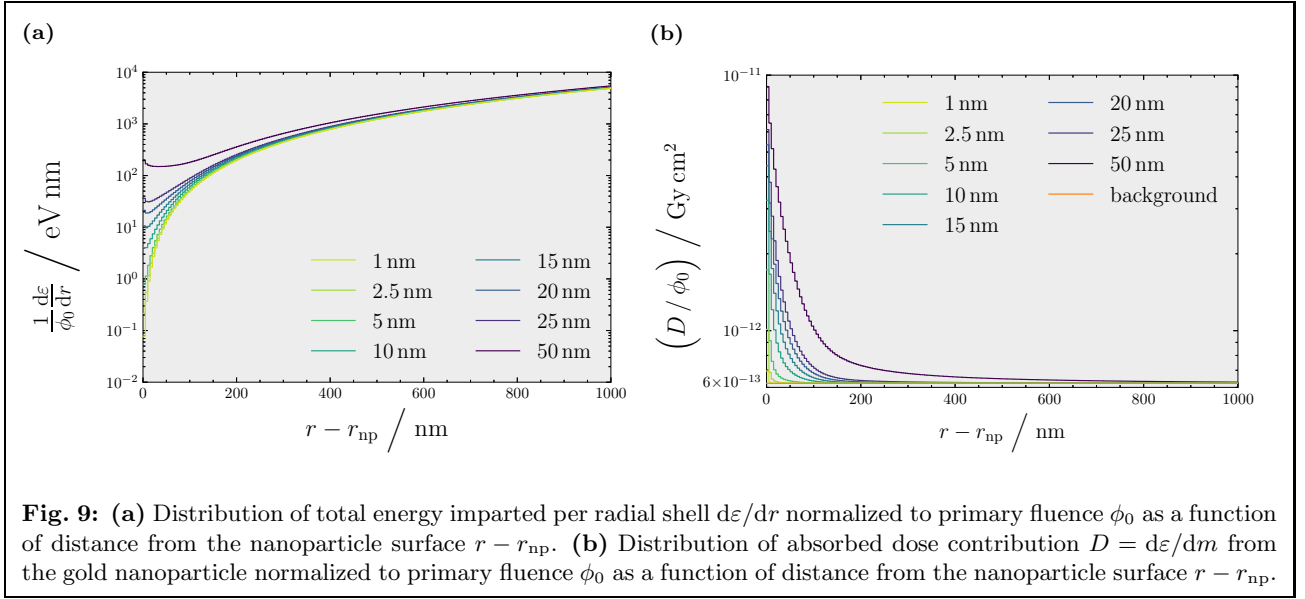
The dose enhancement factor (DEF, also referred to as dose enhancement ratio, DER), defined as the ratio of absorbed dose in a volume surrounding a gold NP to the corresponding absorbed dose in the absence of the gold NP in the same volume, is commonly used to characterize the dosimetric impact of nanoparticles, especially in simulation studies. The EURADOS intercomparison study (Rabus et al., 2021b) reports the enhancement as “deviation of the DER from 1”, $\text{DEF} - 1$. For comparison, this quantity is displayed in Fig. 10. A detailed comparison of the DEFs for nanoparticles of $r_{\text{np}} = 25$ nm and $r_{\text{np}} = 50$ nm can be found in Supplementary Figs. S4(a) and S4(b), respectively⁵.

3.4 Linking ionization clustering to imparted energy and dose

In order to relate ionization clustering to the absorbed dose, a cluster enhancement factor ($\text{CEF}_{N_{F_k}}$) is defined, analogously to the dose enhancement factor (DEF), as the ratio of the frequency of clusters of size $\nu \geq k$ in a volume surrounding a gold NP (or shells around it) to the corresponding frequency in the absence of the gold NP.

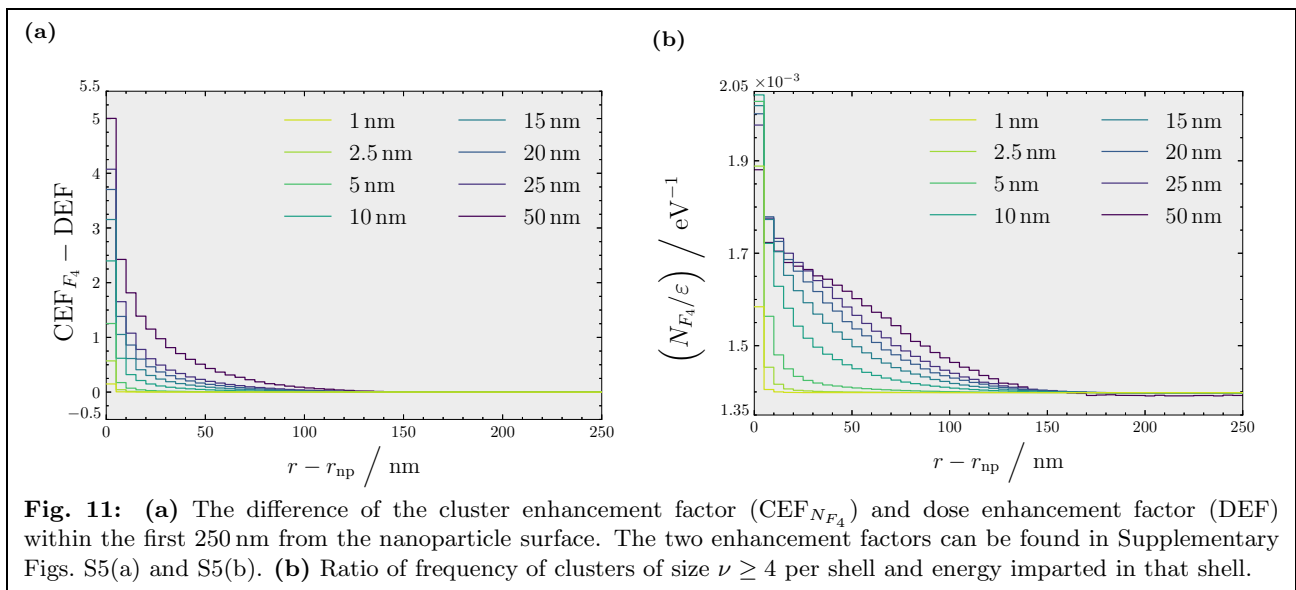
The difference between $\text{CEF}_{N_{F_k}}$ and DEF is reported in Fig. 11(a) and illustrates a relatively increased enhancement of clustering with respect to the enhancement of dose in the shells surrounding the gold NP. This effect is highly localized and largely confined to radial distances up to $\lesssim 50$ nm, albeit quite pronounced. The

⁵ Note that the nanoparticle sizes in Rabus et al. (2021b) are specified as diameters, i.e. a nanoparticle with radius $r_{\text{np}} = 50$ nm is referred to as a “100 nm-nanoparticle”.



enhancement factor of ionization clustering as well as the dose enhancement factor, for comparison, are reported individually in Supplementary Figs. S5(a) and S5(b), respectively.

Fig. 11(b) shows the number of clusters per energy imparted as a function of radial distance from the nanoparticle. Both of these results are consistent with the emission of Auger electrons from the nanoparticle: the energy imparted by these low energy Auger electrons results from a higher number of ionizations.



4 Discussion

Fluence spectra

The photon (and consequentially the electron fluence) impinging on the nanoparticle is influenced by photons scattered back into the region of interest. The extent of this effect depends on the geometry considered. The geometry here has been designed to make the results comparable to the EURADOS intercomparison exercise (Li et al., 2020a,b; Rabus et al., 2021a,b), as outlined in Section 2.2. Here, the total number of photons present in the region of interest is roughly 1.38 times that of primary photons.

Profiting from the two-step simulation scheme, fluence spectra of electrons could be individuated for both photons (Fig. 4) and electrons (Fig. 5(a) and Fig. 5(b)) impinging on the nanoparticle surface. Whereas the electrons produced by electrons are largely independent of NP radius, the photon-produced electron fluence grows roughly linearly with the NP radius and it could be shown that with growing NP-radius, it is electrons produced by incident photons that dominate the fluence of electrons leaving the nanoparticle. The peaks in Fig. 4 have been identified as electrons stemming from Auger transitions. The small range of these electrons is assumed to drive the increase in clustering in the proximity to the NP surface.

The spectral energy fluence of such photon-induced electrons aligns well with the results from the EURADOS intercomparison publication by Li et al. (2024, in press), which has investigated nanoparticles of $r_{\text{np}} = 25$ nm and $r_{\text{np}} = 50$ nm. Comparisons of the spectra are shown in Supplementary Figs. S3(a) and S3(b) for these two NP radii, respectively.

Clustering methods

The associated volume clustering (AVC) approach, initially used to score clusters of energy transfer points, has been used here for the first time to score ionization clusters to assess the physical radiation effect of NPs and at target size equivalent to those considered, for instance, in Grosswendt (2006) and Faddegon et al. (2023). Broadly speaking, this method and other sampling-based methods (Alexander et al., 2015; Ramos-Méndez et al., 2018; Selva et al., 2018) build one of three categories of clustering methods, all of which realize the ten basepair localization criterion mentioned in Section 2.3 in one way or another. The other two categories are 1.) counting ionization-sites within some type of grid (Braunroth et al., 2020; Ngcezu and Rabus, 2021; Rabus et al., 2020) and 2.) density-based clustering such as the Density-Based Spatial Clustering of Applications with Noise (DBSCAN) algorithm, initially developed by Ester et al. (1996) and modified for the estimation of DNA lesion clusters estimated as a random subset of ionizations (Francis et al., 2011).

Unlike uniform sampling, sampling in the AV of a track utilizes each ionization for scoring and thus makes more efficient use of sampled volumes. How much more efficient this is depends on the fraction of the AV and the scoring volume.

While intended use of DBSCAN is not the clustering of ionizations but rather of the (more sparsely distributed) DNA lesions, one of its pathologies is its tendency to form clusters of large spatial dimensions, as it is based on a spatial, pairwise distance measure. Such complex damages extended over volumes larger than a ten basepair DNA segment may comprise many ionizations and their significance to DNA damage is difficult to interpret. The associated volume clustering method avoids this behaviour by design, strictly enforcing a spatial limit to the size of a cluster.

Grid-based approaches (Braunroth et al., 2020; Rabus et al., 2020), e.g. in cylindrical grids, are computationally efficient (with a time complexity of $\mathcal{O}(\bar{N})$, with the expected number \bar{N} of ionization sites of a track). However, AVC, while not solvable in linear time ($\mathcal{O}(\bar{N}^2)^6$), can be utilized with virtually any scoring volume geometry, such as spheres used here or cylinders, which more closely resemble the shape of a DNA segment.

Main findings

Different contributions to ionization clusters were quantified. Together with the scored fluence spectra on the nanoparticle surface, these contributions could reveal information about the physical mechanisms characterizing the gold NP enhancement effect. With growing NP-radius, it is electrons produced by incident photons that dominate the fluence of electrons leaving the nanoparticle and thus the occurrence of ionization clusters.

For larger distances from the surface, the linear density of ionization cluster-frequency (Fig. 6(a)) is dominated by the background contribution. While itself constant throughout space, this contribution grows with the volume of the shell around the nanoparticle (which is roughly proportional to r^2).

A straightforward way to visualize the range of significant increase of ionization clusters is to consider the number of ionization clusters per mass, Fig. 6(b). In this representation, the background contribution is constant. In reminiscence of the energy imparted per mass – the dose – Faddegon et al. (2023) have coined the term ‘cluster dose’ for this quantity.

As worked out in Section 2.4, the primary fluence affects the formation of ionization clusters. The plots of the conditional radial density of clusters (Figs. 8(a) - 8(d)) show the non-linearity introduced by multiple occurrences of photon interactions at different dose levels.

This emphasizes the necessity of considering absolute (i.e. fluence dependent) quantities rather than relative quantities, like enhancement ratios or cluster frequencies per imparted energy, alone. This effect is especially evident for smaller gold NPs, where a shoulder pattern emerges for distances fitting the range of the M shell Auger electrons visible in the photon-generated electron spectrum in Fig. 4.

The results for the energy imparted within the shells around the NPs have been used to calculate absorbed dose as well as dose enhancement factors (DEFs). These DEFs show good agreement with the results from the EURADOS intercomparison (Rabus et al., 2021b) exercise, which have been used to check the results for consistency, see Supplementary Figs. S4(a) and S4(b), for DEFs for nanoparticle radii 25 nm and 50 nm, respectively. It should be noted that only energy imparted by ionizations was scored, whereas the in intercomparison exercise ionizations as well as excitations were scored. This contribution has been found to be 80 % of all energy deposits (Gervais et al., 2006). Another difference worth mentioning is the two-step simulation setup. Simulations conducted within the intercomparison exercise were performed with a circular beam of $d_{\text{np}} + 10$ nm, with the nanoparticle diameter d_{np} . The resulting lack of secondary electron equilibrium was accounted for using the methods detailed in Rabus et al. (2019).

While the occurrence of ionization clusters (Fig. 6(a)) and the energy imparted (Fig. 9(a)) show qualitative similarities, it could be shown that the number of ionization clusters of size $\nu \geq 4$ per imparted energy (Fig. 11(b)) varies with distance and is increased within the first 150 nm from the nanoparticle surface. This enhanced clustering near the NP surface may be the origin of what is described as therapy-activated nanoparticle and immunotherapy (Penninckx et al., 2023). In alignment with this local increase of clustering, the determined cluster enhancement factor (CEF_{F_4}) exceeds the DEF by up to 46 % (for the 10 nm-radius gold NP) (Fig. 11(a)) as well as individually in Supplementary Figs. S5(a) and S5(b)). This highlights the necessity of considering ionization clustering for the characterization of cell damage.

Relevance

Given that in a therapeutic application of gold NPs there is generally a large number of gold NPs present in a tumour cell, the question of the relevance of the present results may be raised. To address this point,

⁶ While this is not a challenge when clustering ionizations from 100 kVp X-rays, this might be a relevant consideration for high-LET radiation.

the following estimates are based on the approach outlined in (Rabus, 2024b). Assume a spatially uniform distribution of gold NPs and a mass fraction of 2% of gold in a cell represented by water. For the photon energy spectrum considered in this work, such a concentration of gold results in an increase of the average absorbed dose by a factor of about 1.8. The corresponding volume fraction of gold NPs is about 10^{-3} such that the ‘associated volume’ of a gold NP (comprising the points in space closer to the gold NP than to its neighbours) has a radius of about ten times the gold NP radius. The nearest neighbour distance is thus about 20 times the gold NP radius. This implies that for this value of mass fraction of gold, the nearest neighbours are outside the region of significant enhancement of ionization clustering (or energy imparted) for the gold NP radii considered here, as can be seen in Fig. 6(b). For uniformly distributed nanoparticles of these sizes, the density of ionization clusters (or energy imparted) can be assumed to be additive. For smaller gold NP radii, the nearest neighbours are within the region of significant increase of ionization clustering and can interact with the electrons emitted from the considered gold NP where a photon interaction occurs.

When the nearest neighbors are located outside of the region of significant clustering there is only a small modification of the spatial density of ionization clusters in the form of a small sink effect that has been observed for larger nanoparticles at distances exceeding 100 nm (Fig. 7) of the neighbouring gold NPs and a localized increase around them (this estimation also holds for the number of ionization clusters per imparted energy, Fig. 11(b)). Hence, the synergistic effects of the gold NPs can also be expected to be additive as well, and this conjecture will be tested in future work. It should be added that according to the review by Kuncic and Lacombe (2018), the maximum concentrations of gold NPs found in radiobiological studies are more than two orders of magnitude smaller than the mass fraction of 2% used in the estimate above. With such concentrations of gold NPs, the nearest neighbour distance for uniform spatial distribution is higher by a factor in the order of 50. Then, neighbours of gold NPs of the smallest radius of 1 nm are also outside the range of significantly increased ionization cluster density. When clustering of nanoparticles occurs (as is often found in radiobiological studies), the preceding argument does not hold and changes due to the close proximity of nearest neighbours will occur as reported in preceding simulation studies (Byrne et al., 2018; Rudek et al., 2019). However, it may still be possible to estimate the respective overall effect by superposition of the effects of a single gold NP reported here, which will also be investigated in further studies.

It is worth mentioning that the presence of further gold NPs in a considered volume of matter not only changes the radiation field of electrons but also that of photons. In the energy range considered in this study, this will be almost exclusively through coherent photon scattering, which contributes on average about 6% of the total interaction coefficient of gold. In addition, there is a small contribution to the photon fluence by fluorescence photons originating in the radiative de-excitation of gold atoms undergoing a core-level photoabsorption⁷.

Caveats and final remarks

The two-step simulation approach entails sampling photons and electrons on the surface of a gold nanoparticle. The assumption made here is that the particles impinging on the nanoparticle are distributed isotropically, which is an approximation. Subsequently cluster frequencies (or other quantities) are considered solely as a function of radial distance, overlooking anisotropies of the distribution of ionization clusters. The anisotropy of photoelectron emission has been studied (Derrien et al., 2023; Rabus, 2024a). The magnitude of the anisotropy of imparted energy under CPE is estimated to be in the few percent range (3.5% for 30 keV photons and 3.9% for 80 keV photons) for a 25 nm-radius target at a distance of 200 nm from the surface (Rabus, 2024a).

The sampling method employed for single incident electrons is grounded on the assumption that these electrons are independent. Of course, this is an approximation that discards synergistic effects of electrons with other electrons from the same primary photon. If the interactions of complete electron tracks with gold NPs were to be considered, their “fluence” would be much smaller than the fluence determined for individual

⁷ In this context, it may be useful to comment on the absence of K shell fluorescence peaks in the photon fluence spectra induced by incident photons (Supplementary Figs. S2(a) and (b)). As can be derived from the evaluated photon data library (Cullen et al., 1997), the probability of a K shell photoabsorption occurring in gold can be estimated to be about 73% in the energy range above the K absorption edge of gold for the photon spectrum used here. According to the evaluated atomic data library (Perkins et al., 1991), the probability of a radiative deexcitation of a K shell vacancy in gold is 95%, where the dominant $K\alpha_1$ line occurs with a probability of about 48%. Therefore, one might expect to see peaks related to fluorescence decay of K shell ionized gold atoms. The main reason for their absence is the use of an energy bin size of 100 eV in the scoring, which significantly reduces the height of any, generally very narrow peaks. Furthermore, averaged over the complete incident photon spectrum, the proportion of K shell absorption to the total photoabsorption cross-section is only about 1.8%. Therefore, the probability of a gold $K\alpha_1$ photon at about 68.805 keV (Perkins et al., 1991) being emitted is only about 0.9%. Accordingly, the content of the corresponding photon energy bin is only increased by this small proportion, which is well below the statistical fluctuations.

electrons. Therefore, a determination of conditional quantities as undertaken for photons would be much more intricate.

While the geometry used in this work has been designed to ensure CPE conditions, photon equilibrium conditions are only met partially: the geometry allows for scoring photons that are scattered back into the scoring volume (region ‘A’ in Fig. 1), although photons scattered at larger angles e.g. laterally into the scoring volume are not accounted for as the chosen photon beam is collimated to the (extended) region of interest (i.e. regions ‘A’ and ‘B’ in Fig. 1). It is assumed that this is a small effect (Rabus et al., 2019) that should be addressed in a future study.

Conditional ionization cluster densities have been determined for photons using the estimates of the mean expected number of ionization interactions for photons that may cause inner-shell ionizations. The probability of an ionizing interaction is considerably larger, when considering low energy ($E \leq 1$ keV) photons. However, the fluence of these photons is negligibly small and these photons are not capable of producing M shell Auger electrons so that their impact is expected to be small.

The simulations in this work have been conducted for gold in water. Gold nanoparticles that have been considered for clinical usage are coated to influence cell uptake and mitigate toxic effects. The effect that such coatings can have on the number of resulting ionization clusters has not been studied here, but will influence low-energy electrons (Belousov et al., 2018, 2019; Morozov et al., 2018; Rabus et al., 2023). The size of nanoparticles used in experiments is also subject to variation due to manufacturing, a source of uncertainty that could be estimated for comparison with experimental data. Finally, although track-structure codes, in principle, allow for highly accurate computations, the uncertainties in the cross-sections used for simulation are assumed to be a major source of uncertainty, most noticeably at low energies (Bug, 2014; Villagrasa et al., 2018, 2022). Especially when investigating clustering caused by such low energy electrons in the proximity of a nanoparticle, the effect of such errors should be gauged.

Conclusions

The simulations in this work have been conducted under charged particle equilibrium conditions as well as using a track structure code for simulation. While previous works have examined the radial dependence of energy imparted around a gold nanoparticle, this work has also determined the frequency of ionization clusters. This methodology as well as the presented validation of the data allow for a thorough systematic evaluation of the gold nanoparticle enhancement effect. The fact that calculations have been conducted under charged particle equilibrium conditions allows for a realistic evaluation of the cluster and dose enhancement factors and the quantitative comparison of the magnitude of these effects.

In fact, the data presented show that the gold NPs enhancement of ionization cluster frequency exceeds that of absorbed dose in the immediate vicinity of the gold NP so that the energy imparted cannot act as a good proxy for increased ionization cluster frequencies and highlights the necessity for nanodosimetric evaluation to understand physical mechanisms behind their radiation effect. The reported conditional radial densities of ionization clustering show a shoulder increasing for smaller nanoparticle radii that – judging from the distance to the surface – can be explained as contributions of the M shell Auger electrons.

The two-step approach in simulation allowed for the individual consideration of the spectral fluences of electrons produced by photons and electrons. For the 100 kVp X-rays studied in this work, the relevant component to clustering has been shown to be the photon field-induced electrons, rather than the electron field itself, which – apart from a small sink effect – is not significantly affected by the gold nanoparticles. A rather important role seems to be the interplay between the production of electrons within the nanoparticle and their capability of leaving it. Nevertheless the electron field is important in determining the background of ionization clusters as well as energy imparted.

As an important driver for both the local increase of ionization clusters per energy imparted and the local increase of the conditional radial densities of ionization clustering for smaller nanoparticle radii, these are found to be mediated by an increase in low-energy electrons consistent with the emission of electrons from M shell Auger transitions as part of the de-excitation cascade from inner-shell-ionized gold atoms.

Acknowledgements

The authors express their gratitude to the dedicated team of the High Performance Cluster of the German National Metrology Institute (PTB) for their ongoing support throughout the production of the data.

This project is part of the programme “Metrology for Artificial Intelligence in Medicine” (M4AIM), which is funded by the Federal Ministry for Economic Affairs and Climate Action (BMWK) within the scope of the “QI-Digital” initiative.

References

- Alexander, F., Villagrasa, C., Rabus, H., and Wilkens, J. J. (2015). Energy dependent track structure parametrisations for protons and carbon ions based on nanometric simulations. *The European Physical Journal D*, 69(9):216.
- Amols, H., Wu, C., and Zaider, M. (1990). On Possible Limitations of Experimental Nanodosimetry. *Radiation Protection Dosimetry*, 31(1-4):125-128.
- Andreo, P., Burns, D. T., and Salvat, F. (2012). On the uncertainties of photon mass energy-absorption coefficients and their ratios for radiation dosimetry. *Physics in Medicine & Biology*, 57(8):2117.
- Bantsar, A., Colautti, P., Conte, V., Hilgers, G., Pietrzak, M., Pszona, S., Rabus, H., and Selva, A. (2017). State of The Art of Instrumentation in Experimental Nanodosimetry. *Radiation Protection Dosimetry*, 180(1-4):177-181.
- Baró, J., Sempau, J., Fernández-Varea, J., and Salvat, F. (1995). PENELOPE: An algorithm for Monte Carlo simulation of the penetration and energy loss of electrons and positrons in matter. *Nuclear Instruments and Methods in Physics Research Section B: Beam Interactions with Materials and Atoms*, 100(1):31-46.
- Belousov, A. V., Morozov, V. N., Krusanov, G. A., Kolyvanova, M. A., Chernyaev, A. P., and Shtil, A. A. (2018). Modeling the Effect of Surface Modification of Gold Nanoparticles Irradiated with ^{60}Co on the Secondary Particles Emission Spectrum. *Doklady Physics*, 63(3):96-99.
- Belousov, A. V., Morozov, V. N., Krusanov, G. A., Kolyvanova, M. A., and Shtil, A. A. (2019). The Effect of Gold Nanoparticle Surface Modification with Polyethylene Glycol on the Absorbed Dose Distribution upon Irradiation with ^{137}Cs and ^{60}Co Photons. *Biophysics*, 64(1):23-30.
- Berger, M., Hubbell, J., Seltzer, S., Chang, J., Coursey, J., Sukumar, R., Zucker, D., and Olsen, K. (2010). XCOM: Photon Cross Section Database (version 1.5).
- Bernal, M. A., Bordage, M. C., Brown, J. M. C., Davidková, M., Delage, E., Bitar, Z. E., Enger, S. A., Francis, Z., Guatelli, S., Ivanchenko, V. N., Karamitros, M., Kyriakou, I., Maigne, L., Meylan, S., Murakami, K., Okada, S., Payno, H., Perrot, Y., Petrovic, I., Pham, Q. T., Ristic-Fira, A., Sasaki, T., Štěpán, V., Tran, H. N., Villagrasa, C., and Incerti, S. (2015). Track structure modeling in liquid water: A review of the Geant4-DNA very low energy extension of the Geant4 Monte Carlo simulation toolkit. *Physica Medica: European Journal of Medical Physics*, 31(8):861-874.
- Braunroth, T., Nettelbeck, H., Ngcezu, S. A., and Rabus, H. (2020). Three-dimensional nanodosimetric characterisation of proton track structure. *Radiation Physics and Chemistry*, 176:109066.
- Brice, D. (1984). ICRU Report 37: Stopping powers for electrons and positrons. page 271.
- Brivio, D., Nguyen, P. L., Sajo, E., Ngwa, W., and Zygmanski, P. (2017). A Monte Carlo study of I-125 prostate brachytherapy with gold nanoparticles: dose enhancement with simultaneous rectal dose sparing via radiation shielding. *Physics in Medicine & Biology*, 62(5):1935.
- Brun, R. and Rademakers, F. (1997). ROOT — An object oriented data analysis framework. *Nuclear Instruments and Methods in Physics Research Section A: Accelerators, Spectrometers, Detectors and Associated Equipment*, 389(1):81-86. New Computing Techniques in Physics Research V.
- Bug, M. U. (2014). Nanodosimetric particle track simulations in water and DNA media.
- Byrne, H., McNamara, A., and Kuncic, Z. (2018). Impact of nanoparticle clustering on dose radio-enhancement. *Radiation Protection Dosimetry*, 183(1-2):50-54.
- Cullen, D. E., Hubbell, J. H., and Kissel, L. (1997). EPDL97: the evaluated photo data library '97 version.
- Derrien, J., Pauly, N., Adam, J.-F., and Reniers, B. (2023). Investigation of the anisotropic distribution of microdosimetric quantities in the vicinity of X-ray-irradiated gold nanoparticles. *Radiation Physics and Chemistry*, 213:111232.
- Ester, M., Kriegel, H. P., Sander, J., and Xiaowei, X. (1996). A density-based algorithm for discovering clusters in large spatial databases with noise. *Proceedings of 2nd International Conference on Knowledge Discovery and Data Mining (KDD-96)*.

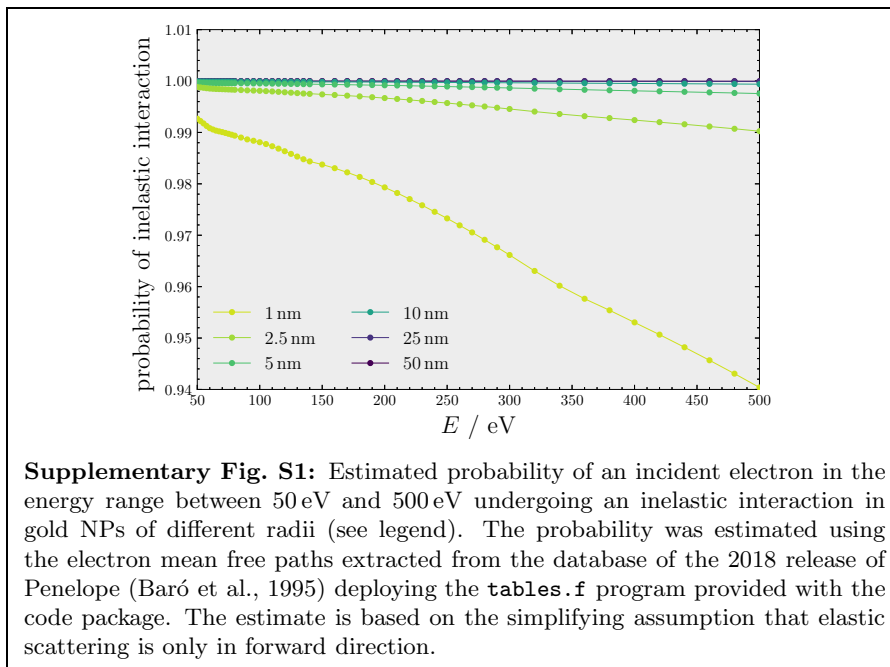
- Faddegon, B., Blakely, E. A., Burigo, L., Censor, Y., Dokic, I., Kondo, N. D., Ortiz, R., Méndez, J. R., Rucinski, A., Schubert, K., Wahl, N., and Schulte, R. (2023). Ionization detail parameters and cluster dose: a mathematical model for selection of nanodosimetric quantities for use in treatment planning in charged particle radiotherapy. *Physics in Medicine & Biology*, 68(17):175013.
- Francis, Z., Villagrasa, C., and Clairand, I. (2011). Simulation of DNA damage clustering after proton irradiation using an adapted DBSCAN algorithm. *Computer Methods and Programs in Biomedicine*, 101(3):265–270.
- Gadoue, S. M., Zygmanski, P., and Sajo, E. (2018). The dichotomous nature of dose enhancement by gold nanoparticle aggregates in radiotherapy. *Nanomedicine*, 13(8):809–823.
- Gervais, B., Beuve, M., Olivera, G. H., and Galassi, M. E. (2006). Numerical simulation of multiple ionization and high LET effects in liquid water radiolysis. *Radiation Physics and Chemistry*, 75(4):493–513.
- Gonon, G., Villagrasa, C., Voisin, P., Meylan, S., Bueno, M., Benadjaoud, M. A., Tang, N., Langner, F., Rabus, H., Barquinero, J.-F., Giesen, U., and Gruel, G. (2019). From Energy Deposition of Ionizing Radiation to Cell Damage Signaling: Benchmarking Simulations by Measured Yields of Initial DNA Damage after Ion Microbeam Irradiation. *Radiation Research*, 191(6):566–584.
- Goodhead, D. (1994). Initial Events in the Cellular Effects of Ionizing Radiations: Clustered Damage in DNA. *International Journal of Radiation Biology*, 65(1):7–17.
- Goodhead, D. T. (2006). Energy deposition stochastics and track structure: what about the target? *Radiation Protection Dosimetry*, 122(1–4):3–15.
- Grosswendt, B. (2006). Nanodosimetry, the metrological tool for connecting radiation physics with radiation biology. *Radiation Protection Dosimetry*, 122(1–4):404–414.
- Hainfeld, J. F., Smilowitz, H. M., O’Connor, M. J., Dilmanian, F. A., and Slatkin, D. N. (2013). Gold nanoparticle imaging and radiotherapy of brain tumors in mice. *Nanomedicine (London, England)*, 8(10):1601–1609.
- Hill, M. (2020). Radiation Track Structure: How the Spatial Distribution of Energy Deposition Drives Biological Response. *Clinical Oncology*, 32(2):75–83.
- Incerti, S., Baldacchino, G., Bernal, M., Capra, R., Champion, C., Francis, Z., Guèye, P., Mantero, A., Mascialino, B., Moretto, P., Nieminen, P., Villagrasa, C., and Zacharatou, C. (2010a). The GEANT4-DNA Project. *International Journal of Modeling, Simulation, and Scientific Computing*, 01(02):157–178.
- Incerti, S., Ivanchenko, A., Karamitros, M., Mantero, A., Moretto, P., Tran, H. N., Mascialino, B., Champion, C., Ivanchenko, V. N., Bernal, M. A., Francis, Z., Villagrasa, C., Baldacchino, G., Guèye, P., Capra, R., Nieminen, P., and Zacharatou, C. (2010b). Comparison of Geant4 very low energy cross section models with experimental data in water. *Medical Physics*, 37(9):4692–4708.
- Incerti, S., Kyriakou, I., Bernal, M. A., Bordage, M. C., Francis, Z., Guatelli, S., Ivanchenko, V., Karamitros, M., Lampe, N., Lee, S. B., Meylan, S., Min, C. H., Shin, W. G., Nieminen, P., Sakata, D., Tang, N., Villagrasa, C., Tran, H. N., and Brown, J. M. C. (2018). Geant4-DNA example applications for track structure simulations in liquid water: A report from the Geant4-DNA Project. *Medical Physics*, 45(8):e722–e739.
- Kase, K. R., Bjarngard, B. E., and Attix, F. H. (1985). *The dosimetry of ionizing radiation. Volume 1*. Academic Press Inc.
- Klapproth, A. P., Schuemann, J., Stangl, S., Xie, T., Li, W. B., and Multhoff, G. (2021). Multi-scale Monte Carlo simulations of gold nanoparticle-induced DNA damages for kilovoltage X-ray irradiation in a xenograft mouse model using TOPAS-nBio. *Cancer Nanotechnology*, 12(1):27.
- Koger, B. and Kirkby, C. (2016). A method for converting dose-to-medium to dose-to-tissue in Monte Carlo studies of gold nanoparticle-enhanced radiotherapy. *Physics in Medicine & Biology*, 61(5):2014–2024. Publisher: IOP Publishing.
- Kolyvanova, M. A., Belousov, A. V., Krusanov, G. A., Isagulieva, A. K., Morozov, K. V., Kartseva, M. E., Salpagarov, M. H., Krivoshapkin, P. V., Dement’eva, O. V., Rudoy, V. M., and Morozov, V. N. (2021). Impact of the Spectral Composition of Kilovoltage X-rays on High- Z Nanoparticle-Assisted Dose Enhancement. *International Journal of Molecular Sciences*, 22(11):6030.
- Kuncic, Z. and Lacombe, S. (2018). Nanoparticle radio-enhancement: principles, progress and application to cancer treatment. *Physics in Medicine & Biology*, 63(2):02TR01.
- Li, W., Beuve, M., Di Maria, S., Friedland, W., Heide, B., Klapproth, A., Li, C., Pognant, F., Rabus, H., Rudek, B., Schuemann, J., and Villagrasa, C. (2020a). Corrigendum to “Intercomparison of dose enhancement ratio and secondary electron spectra for gold nanoparticles irradiated by X-rays calculated using multiple Monte Carlo simulation codes” [Phys. Med. 69 (2020) 147–163]. *Physica Medica*, 80:383–388.
- Li, W. B., Belchior, A., Beuve, M., Chen, Y. Z., Di Maria, S., Friedland, W., Gervais, B., Heide, B., Hocine, N., Ipatov, A., Klapproth, A. P., Li, C. Y., Li, J. L., Multhoff, G., Pognant, F., Qiu, R., Rabus, H., Rudek, B., Schuemann, J., Stangl, S., Testa, E., Villagrasa, C., Xie, W. Z., and Zhang, Y. B. (2020b). Intercomparison of dose enhancement ratio and secondary electron spectra for gold nanoparticles irradiated by X-rays calculated using multiple Monte Carlo simulation codes. *Physica medica: PM: an international journal devoted to the applications of physics to medicine and biology: official journal of the Italian Association of Biomedical Physics (AIFB)*, 69:147–163.

- Lin, Y., McMahon, S. J., Scarpelli, M., Paganetti, H., and Schuemann, J. (2014). Comparing gold nano-particle enhanced radiotherapy with protons, megavoltage photons and kilovoltage photons: a Monte Carlo simulation. *Physics in Medicine & Biology*, 59(24):7675–7689.
- Lin, Y., Paganetti, H., McMahon, S. J., and Schuemann, J. (2015). Gold nanoparticle induced vasculature damage in radiotherapy: Comparing protons, megavoltage photons, and kilovoltage photons. *Medical Physics*, 42(10):5890–5902. Publisher: Wiley.
- Lomax, M. E., Folkes, L. K., and O’Neill, P. (2013). Biological Consequences of Radiation-induced DNA Damage: Relevance to Radiotherapy. *Clinical Oncology*, 25(10):578–585.
- Lorat, Y., Brunner, C. U., Schanz, S., Jakob, B., Taucher-Scholz, G., and Rube, C. E. (2015). Nanoscale analysis of clustered DNA damage after high-LET irradiation by quantitative electron microscopy – The heavy burden to repair. *DNA Repair*, 28:93–106.
- McMahon, S. J., Hyland, W. B., Muir, M. F., Coulter, J. A., Jain, S., Butterworth, K. T., Schettino, G., Dickson, G. R., Hounsell, A. R., O’Sullivan, J. M., Prise, K. M., Hirst, D. G., and Currell, F. J. (2011). Biological consequences of nanoscale energy deposition near irradiated heavy atom nanoparticles. *Scientific Reports*, 1(1):18.
- Mesbahi, A. (2010). A review on gold nanoparticles radiosensitization effect in radiation therapy of cancer. *Reports of Practical Oncology & Radiotherapy*, 15(6):176–180.
- Moradi, F., Saraee, K. R. E., Sani, S. F. A., and Bradley, D. A. (2020). Metallic nanoparticle radiosensitization: The role of Monte Carlo simulations towards progress. *Radiation Physics and Chemistry*, page 109294.
- Morozov, V. N., Belousov, A. V., Krusanov, G. A., Kolyvanova, M. A., Chernyaev, A. P., and Shtil, A. A. (2018). Secondary Electron Spectral Changes of Irradiated Gold Nanoparticle Caused By PEGylation. *KnE Energy*, 3(2):278.
- Ngcezu, S. A. and Rabus, H. (2021). Investigation into the foundations of the track-event theory of cell survival and the radiation action model based on nanodosimetry. *Radiation and Environmental Biophysics*, 60(4):559–578. arXiv:2105.07159 [physics.med-ph].
- Penninckx, S., Thariat, J., and Mirjolet, C. (2023). Chapter Six - Radiation therapy-activated nanoparticle and immunotherapy: The next milestone in oncology? In Mirjolet, C. and Galluzzi, L., editors, *Ionizing Radiation and the Immune Response - Part B*, volume 378 of *International Review of Cell and Molecular Biology*, pages 157–200. Academic Press.
- Perkins, S., Cullen, D., Chen, M., Rathkopf, J., Scofield, J., and Hubbell, J. (1991). Tables and graphs of atomic subshell and relaxation data derived from the LLNL Evaluated Atomic Data Library (EADL), Z= 1–100. Technical report, Lawrence Livermore National Lab.(LLNL), Livermore, CA (United States).
- Poignant, F., Monini, C., Testa, E., and Beuve, M. (2021). Influence of gold nanoparticles embedded in water on nanodosimetry for keV photon irradiation. *Medical Physics*, 48(4):1874–1883.
- Rabus, H. (2024a). Comment on “Investigation of the anisotropic distribution of microdosimetric quantities in the vicinity of X-ray-irradiated gold nanoparticles” by Derrien et al. [*Radiation Physics and Chemistry* 213, 111232 (2023)]. *Radiation Physics and Chemistry*, 216:111466.
- Rabus, H. (2024b). Comment on “Reproducibility study of Monte Carlo simulations for nanoparticle dose enhancement and biological modeling of cell survival curves” by Velten et al [*Biomed Phys Eng Express* 2023;9:045004]. *Biomedical Physics & Engineering Express*, 10(2):028002.
- Rabus, H., Gargioni, E., Li, W. B., Nettelbeck, H., and Villagrasa, C. (2019). Determining dose enhancement factors of high-Z nanoparticles from simulations where lateral secondary particle disequilibrium exists. *Physics in Medicine & Biology*, 64(15):155016.
- Rabus, H., Hepperle, P., Schlueter, C., Hloskovsky, A., and Baek, W. Y. (2023). Experimental benchmark data for Monte Carlo simulated radiation effects of gold nanoparticles. Part I: Experiment and raw data analysis. *Physica Scripta*, 98(5):055015.
- Rabus, H., Li, W. B., Nettelbeck, H., Schuemann, J., Villagrasa, C., Beuve, M., Di Maria, S., Heide, B., Klapproth, A. P., Poignant, F., Qiu, R., and Rudek, B. (2021a). Consistency checks of results from a Monte Carlo code intercomparison for emitted electron spectra and energy deposition around a single gold nanoparticle irradiated by X-rays. *Radiation Measurements*, 147:106637.
- Rabus, H., Li, W. B., Villagrasa, C., Schuemann, J., Hepperle, P. A., de la Fuente Rosales, L., Beuve, M., Maria, S. D., Klapproth, A. P., Li, C. Y., Poignant, F., Rudek, B., and Nettelbeck, H. (2021b). Intercomparison of Monte Carlo calculated dose enhancement ratios for gold nanoparticles irradiated by X-rays: Assessing the uncertainty and correct methodology for extended beams. *Physica Medica*, 84(1):241–253.
- Rabus, H., Ngcezu, S. A., Braunroth, T., and Nettelbeck, H. (2020). “Broadscale“ nanodosimetry: Nanodosimetric track structure quantities increase at distal edge of spread-out proton Bragg peaks. *Radiation Physics and Chemistry*, 166:108515.
- Ramos-Méndez, J., Burigo, L. N., Schulte, R., Chuang, C., and Faddegon, B. (2018). Fast calculation of nanodosimetric quantities in treatment planning of proton and ion therapy. *Physics in Medicine & Biology*, 63(23):235015.
- Rucinski, A., Biernacka, A., and Schulte, R. (2021). Applications of nanodosimetry in particle therapy planning and beyond. *Physics in Medicine & Biology*, 66(24):24TR01.

- Rudek, B., McNamara, A., Ramos-Méndez, J., Byrne, H., Kuncic, Z., and Schuemann, J. (2019). Radio-enhancement by gold nanoparticles and their impact on water radiolysis for X-ray, proton and carbon-ion beams. *Physics in Medicine & Biology*, 64(17):175005.
- Sakata, D., Kyriakou, I., Tran, H. N., Bordage, M.-C., Rosenfeld, A., Ivanchenko, V., Incerti, S., Emfietzoglou, D., and Guatelli, S. (2019). Electron track structure simulations in a gold nanoparticle using Geant4-DNA. *Physica Medica*, 63:98–104.
- Seltzer, S. M., Bartlett, D. T., Burns, D. T., Dietze, G., Menzel, H.-G., Paretzke, H. G., and Wambersie, A. (2011). ICRU Report 85: Fundamental Quantities and Units for Ionizing Radiation. *Journal of the ICRU*, 11(1):1–38.
- Selva, A., Conte, V., and Colautti, P. (2018). A Monte Carlo tool for multi-target nanodosimetry. *Radiation Protection Dosimetry*, 180(1-4):182–186.
- Velten, C. and Tome, W. A. (2023). Reproducibility study of Monte Carlo simulations for nanoparticle dose enhancement and biological modeling of cell survival curves. *Biomedical Physics & Engineering Express*, 9:045004.
- Villagrasa, C., Bordage, M. C., Bueno, M., Bug, M., Chiriotti, S., Gargioni, E., Heide, B., Nettelbeck, H., Parisi, A., and Rabus, H. (2018). Assessing the contribution of cross-sections to the uncertainty of Monte Carlo calculations in Micro- and Nanodosimetry. *Radiation Protection Dosimetry*, 183(1-2):11–16.
- Villagrasa, C., Rabus, H., Baiocco, G., Perrot, Y., Parisi, A., Struelens, L., Qiu, R., Beuve, M., Poignant, F., Pietrzak, M., and Nettelbeck, H. (2022). Intercomparison of micro- and nanodosimetry Monte Carlo simulations: An approach to assess the influence of different cross-sections for low-energy electrons on the dispersion of results. *Radiation Measurements*, 150:106675.
- Vlastou, E., Diamantopoulos, S., and Efstathopoulos, E. P. (2020). Monte Carlo studies in Gold Nanoparticles enhanced radiotherapy: The impact of modelled parameters in dose enhancement. *Physica Medica*, 80:57–64.
- Vozenin, M.-C., Hendry, J., and Limoli, C. (2019). Biological Benefits of Ultra-high Dose Rate FLASH Radiotherapy: Sleeping Beauty Awoken. *Clinical Oncology*, 31(7):407–415.
- Walker, A. J. (1977). An Efficient Method for Generating Discrete Random Variables with General Distributions. *ACM Transactions on Mathematical Software*, 3(3):253–256.
- Zygmanski, P., Liu, B., Tsiamas, P., Cifter, F., Petersheim, M., Hesser, J., and Sajo, E. (2013). Dependence of Monte Carlo microdosimetric computations on the simulation geometry of gold nanoparticles. *Physics in Medicine & Biology*, 58(22):7961–7977. Publisher: IOP Publishing.
- Zygmanski, P. and Sajo, E. (2016). Nanoscale radiation transport and clinical beam modeling for gold nanoparticle dose enhanced radiotherapy (GNPT) using X-rays. *British Journal of Radiology*, 89(1059):20150200.

Supplementary Material

Inelastic interaction probability in gold



Probability of photon interactions in a gold NP

Supplementary Table S1: Estimates of the probability of a photon interaction taking place calculated via the linear attenuation coefficient as detailed in Eq. 10 as well as over the loss of photons within the gold NP obtained from the simulation as detailed in Eq. 11. The fluence of photons leaving the nanoparticle used in this estimate is depicted in Supplementary Fig. S2(b).

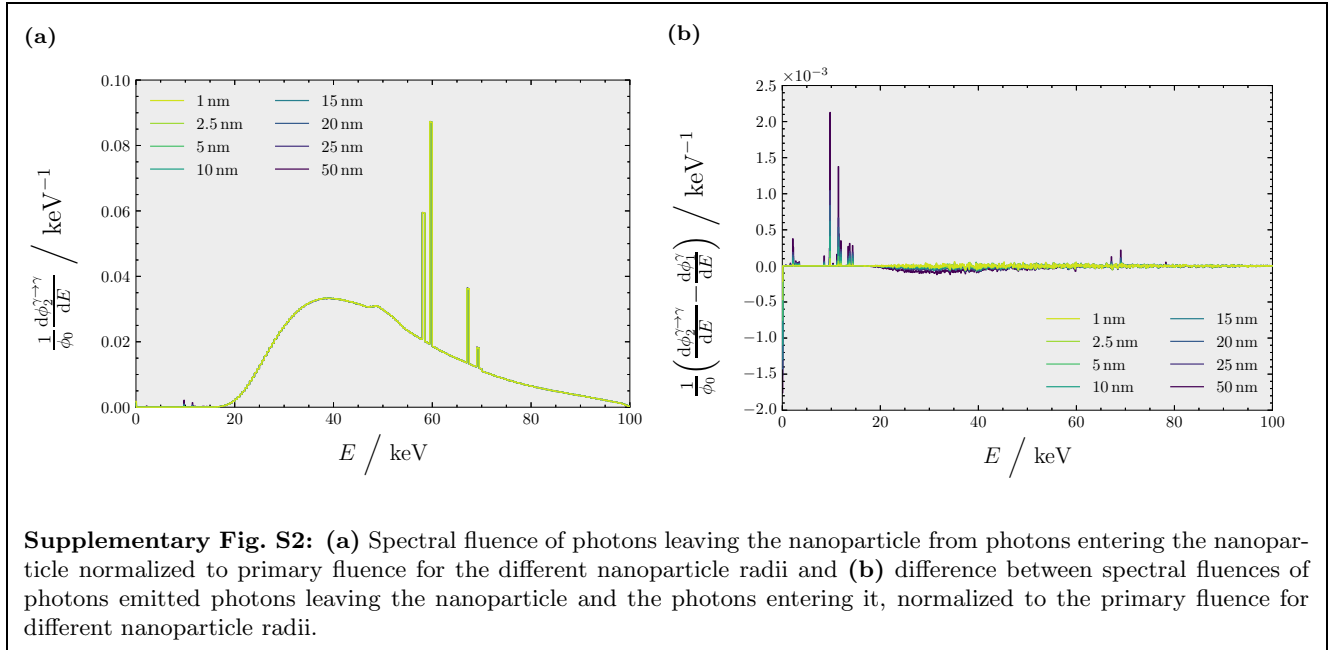
r_{np}	$\langle p_i^\gamma \rangle$ (Eq. 10)	$\langle p_i^\gamma \rangle$ (Eq. 11)	rel. diff.
1 nm	3.02×10^{-5}	2.94×10^{-5}	2.94 %
2.5 nm	7.56×10^{-5}	7.36×10^{-5}	2.75 %
5 nm	1.51×10^{-4}	1.48×10^{-4}	2.33 %
10 nm	3.02×10^{-4}	2.93×10^{-4}	3.14 %
15 nm	4.54×10^{-4}	4.41×10^{-4}	2.86 %
20 nm	6.05×10^{-4}	5.87×10^{-4}	3.00 %
25 nm	7.56×10^{-4}	7.35×10^{-4}	2.91 %
50 nm	1.51×10^{-3}	1.47×10^{-3}	3.04 %

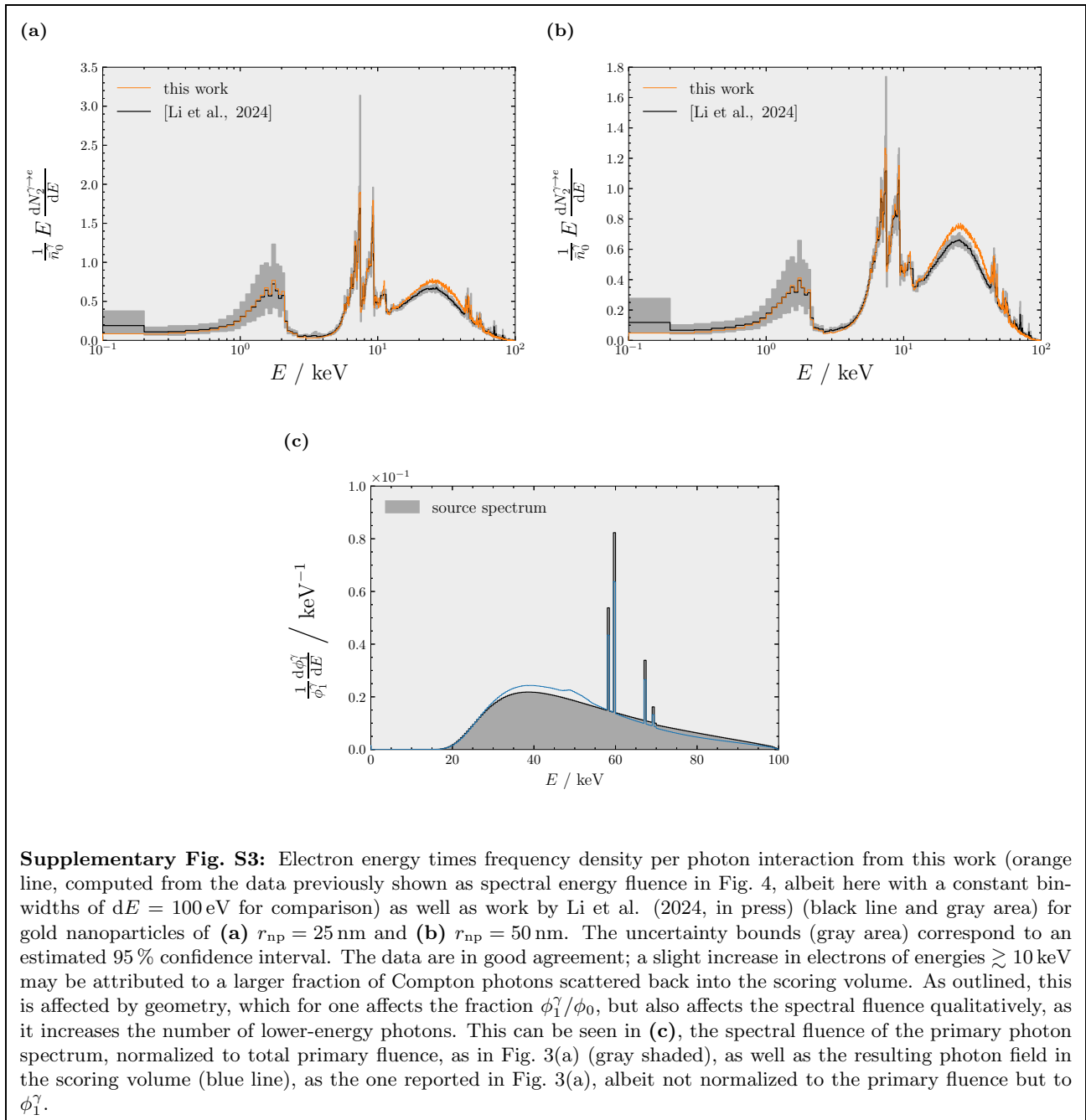
Notation

Supplementary Table S2: Summary of quantities used

Quantity	Description
ϕ	(Integral) fluence (defined in Eq. 5)
$\frac{d\phi}{dE}$	Spectral fluence
$E \frac{d\phi}{dE}$	Spectral energy fluence
ϕ_1^s	Fluence of particle of type s produce by first simulation
$\phi_2^{s \rightarrow s'}$	Fluence of particles of type s' produced by a particle of type s entering the NP simulation
$\bar{n}^\gamma(r_{np}, \phi) / \phi$	Mean number of photon interactions per fluence for a given fluence ϕ (defined in Eq. 12)
N_{F_k}	Number of ionization clusters of size $\nu \geq k$
$(N_{F_k})_{net}^{e \rightarrow e}$	Net gold contribution to the number of ionization clusters of size $\nu \geq k$ considering only those created by electrons created by electrons (defined in Eq.9)
$\langle p_i^\gamma \rangle_{\phi_1^\gamma}$	Probability of a photon ionization within a gold NP (defined in Eq. 10)
$(N_{F_k})_C^\gamma$	Net gold contribution to the number of ionization clusters of size $\nu \geq k$ conditional on a photon interaction occurring within the gold NP (defined in Eq. 16)
ε	Energy imparted
D	Absorbed dose, defined as energy imparted per mass $D = \frac{d\varepsilon}{dm}$
DEF	Dose enhancement factor, the ratio of absorbed dose in a volume surrounding a gold NP to the absorbed dose in the absence of the gold NP
CEF_{F_k}	Clustering enhancement factor, defined as the ratio of frequency of clusters of size $\nu \geq k$ in a volume surrounding a gold NP to the frequency of such clusters in the absence of the gold NP

Fluence spectra

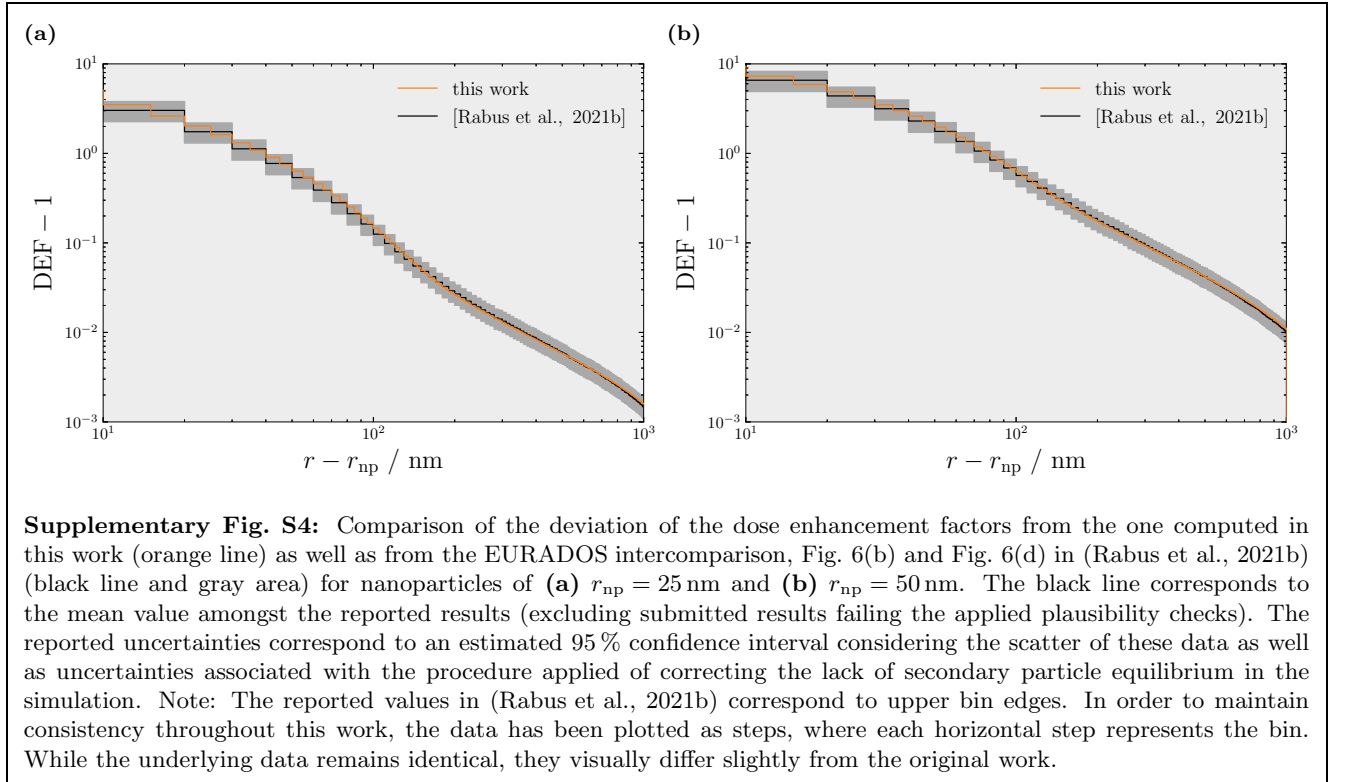


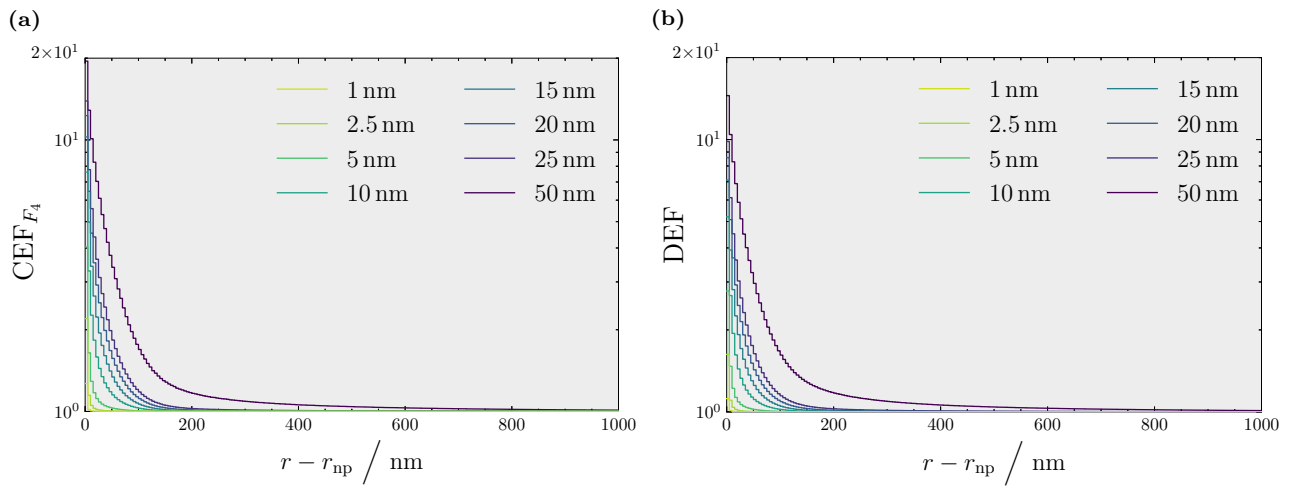


Supplementary Table S3: Ratios of the integral fluence of emitted electrons produced by photons to that of electrons produced by electrons for different gold NP radii and the same primary fluence for different energy ranges. While the ratio increases proportional to the NP radius for photoelectrons ($E \geq 11.5$) and almost proportional for to radius for L shell Auger electrons the ($5.5 \text{ keV} \leq E < 11.5 \text{ keV}$), the increase at energies corresponding to M shell Auger electrons ($500 \text{ eV} \leq E < 5.5 \text{ keV}$) and at energies below 500 eV shows a sub-linear dependence on NP radius

r_{np}	$\phi_2^{\gamma \rightarrow e} / \phi_2^{e \rightarrow e}$				
	$E < 500 \text{ eV}$	$500 \text{ eV} \leq E < 5.5 \text{ keV}$	$5.5 \text{ keV} \leq E < 11.5 \text{ keV}$	$E \geq 11.5 \text{ keV}$	all
1 nm	6.36	2.90	0.77	0.21	1.43
2.5 nm	8.76	6.93	1.91	0.52	2.44
5 nm	10.72	12.72	3.81	1.05	3.79
10 nm	13.53	20.11	7.69	2.10	5.99
15 nm	15.02	23.48	11.57	3.14	7.63
20 nm	16.19	25.59	15.48	4.21	9.13
25 nm	17.09	27.46	19.29	5.28	10.55
50 nm	20.32	34.98	35.87	10.52	16.94

Enhancement Factors





Supplementary Fig. S5: (a) Enhancement factor of clusters of size $\nu \geq 4$, defined analogously to the DEF as the ratio of cluster frequency compared to the cluster frequency in the absence of the gold NP. (b) Dose enhancement factor (DEF), defined as the ratio of absorbed dose surrounding a NP (here in a sphere) to the dose in the absence of the gold NP.